Meteoritics & Planetary Science 38, Nr 11, 1551–1578 (2003)
Abstract available online at http://meteoritics.org

The shape and appearance of craters formed by oblique impact on the Moon and Venus

Robert R. HERRICK[1*] and Nancy K. FORSBERG-TAYLOR[2†]

[1]Lunar and Planetary Institute, 3600 Bay Area Boulevard, Houston, Texas 77058, USA
[2]Department of Geology, Hofstra University, Hempstead, New York 11550, USA
[†]Present Address: Department of Earth and Planetary Sciences, Washington University in St. Louis, One Brookings Drive, Campus Box 1169, St. Louis, Missouri 63130, USA
[*]Corresponding author. E-mail: herrick@lpi.usra.edu

(Received 23 August 2002; revision accepted 12 November 2003)

Abstract–We surveyed the impact crater populations of Venus and the Moon, dry targets with and without an atmosphere, to characterize how the 3-dimensional shape of a crater and the appearance of the ejecta blanket varies with impact angle. An empirical estimate of the impact angle below which particular phenomena occur was inferred from the cumulative percentage of impact craters exhibiting different traits. The results of the surveys were mostly consistent with predictions from experimental work. Assuming a $\sin^2\Theta$ dependence for the cumulative fraction of craters forming below angle Θ, on the Moon, the following transitions occur: <~45 degrees, the ejecta blanket becomes asymmetric; <~25 degrees, a forbidden zone develops in the uprange portion of the ejecta blanket, and the crater rim is depressed in that direction; <~15 degrees, the rim becomes saddle-shaped; <~10 degrees, the rim becomes elongated in the direction of impact and the ejecta forms a "butterfly" pattern. On Venus, the atmosphere causes asymmetries in the ejecta blanket to occur at higher impact angles. The transitions on Venus are: <~55 degrees, the ejecta becomes heavily concentrated downrange; <~40 degrees, a notch in the ejecta that extends to the rim appears, and as impact angle decreases, the notch develops into a larger forbidden zone; <~10 degrees, a fly-wing pattern develops, where material is ejected in the crossrange direction but gets swept downrange. No relationship between location or shape of the central structure and impact angle was observed on either planet. No uprange steepening and no variation in internal slope or crater depth could be associated with impact angle on the Moon. For both planets, as the impact angle decreases from vertical, first the uprange and then the downrange rim decreases in elevation, while the remainder of the rim stays at a constant elevation. For craters on Venus <~15 km in diameter, a variety of crater shapes are observed because meteoroid fragment dispersal is a significant fraction of crater diameter. The longer path length for oblique impacts causes a correlation of clustered impact effects with oblique impact effects. One consequence of this correlation is a shallowing of the crater with decreasing impact angle for small craters.

INTRODUCTION AND BACKGROUND

For planetary impactors approaching from random directions. the frequency function dP for the zenith angle of incidence (Θ) is (Shoemaker 1962):

$$dP = \sin 2\Theta \, d\Theta \quad (1)$$

This equation dictates that virtually all impact craters on the terrestrial planets result from nonvertical impacts, that half of all bodies impacting a planetary surface strike the surface at Θ <45°, and that one-fourth of all impacts occur at Θ <30°. Understanding how the cratering process changes for distinctly nonvertical impacts, or "oblique impacts," is, therefore, critical to understanding planetary impact crater formation and to using the cratering record to study the geologic history of a planet. Absolute age dates are often assigned to planetary surfaces by impact crater counts (e.g., Hartmann 1999; McKinnon et al. 1997; Shoemaker and Wolfe 1982), and the relationship between meteoroid flux and crater size distribution depends, among other variables, on how impact angle affects crater diameter. Craters can be used as probes of crustal material by virtue of their excavation of subsurface material (e.g., Barlow and Bradley 1990; Hörz et al. 1991), and the depth of excavation for a given crater diameter may be affected by impact angle.

Substantial laboratory and theoretical work have been conducted to explore the oblique impact process (see review paper by Pierazzo and Melosh [2000] for a summary of oblique impact studies). That work has been used to make predictions about the shape, size, and morphology of oblique impact craters on the planets. However, only cursory observational studies of the morphology of planetary oblique impacts have been done (Gault and Wedekind 1978, hereafter referred to as GW78; Schultz and Lutz-Garihan 1982; Schultz 1992c), and little work has been done characterizing their topography. The result is that many important aspects of oblique impact are accepted as being understood despite minimal "ground-truth" confirmation with planetary observations. Here, we present observations of impact craters on Venus and the Moon designed to characterize the change of crater shape and morphology with impact angle on those bodies.

A number of laboratory experiments have been conducted to simulate oblique impact under conditions relevant to planetary impact craters. While the specifics of the observed phenomena are dependent on a variety of experimental conditions, some generalities can be drawn from the results. Impact craters larger than a few hundred meters in diameter on the Moon and Venus occur in the "gravity regime" (e.g., Housen et al. 1983) so that the most appropriate laboratory simulations are hypervelocity impacts into a strengthless medium such as sand or pumice. GW78 summarized a number of experiments on the effects of hypervelocity oblique impact in a vacuum. They found that, for impact angles $\Theta <\sim 45°$ with respect to horizontal, the ejecta blanket becomes asymmetric with ejecta lacking in the uprange direction. For $\Theta <\sim 30°$, the downrange ejecta also becomes sparse. At $\Theta <\sim 15°$, a "forbidden zone" occurs uprange where essentially no ejecta exist. For $\Theta <\sim 10°$, the planform of the crater begins to become noncircular and elongated in the direction of projectile travel, and this transition angle seems to be largely independent of target or impactor properties. For $\Theta <\sim 5°$, a full "butterfly pattern" is observable in the ejecta with forbidden zones in both the uprange and downrange direction. At very low angles, a significant portion of the impactor may ricochet off the surface and produce a second crater downrange.

GW78 also measured the topographic shape of the laboratory craters. They found that the depth/diameter ratio was invariable even for quite low impact angles. The mass displaced was proportional to $\sin\Theta$, indicating that only the vertical component of the projectile velocity vector was important in determining final crater size. For $\Theta <\sim 30°$, the crater floor steepened in the uprange direction and the uprange crater rim became lower than the remainder of the rim. At $\Theta <\sim 5°$, the topography became saddle-shaped with negligible rims in both the uprange and downrange direction.

Cratering efficiency, crater shape, and ejecta emplacement in laboratory craters are all strongly affected by the presence of an atmosphere (e.g., Schultz 1992a, b, c). A general increase occurs in the angle for which the various oblique impact effects appear (Schultz 1992b, c), and the ejecta curtain becomes more of an ejecta cloud. The tilting of the ejecta curtain tends to "roll" the ejecta cloud downrange in the presence of an atmosphere. The cloud can also be blown by the trailing wake of the projectile. The downrange momentum of the cloud will cause the various ejecta structures that emerge, such as ramparts and ejecta blankets, to be enhanced downrange. For example, the butterfly pattern that occurs in a vacuum becomes more of a Vshaped "fly-wing" pattern where the butterfly wings become rounded uprange (head of the fly) and swept downrange. Under high atmospheric pressures in the laboratory, asymmetries in the ejecta blanket begin to occur at angles as high as $\Theta = 60°$, with an uprange avoidance zone occuring at $\Theta <\sim 30°$ (Schultz 1992b, c). The fly-wing pattern and elongation of the crater cavity occur for $\Theta <\sim 10°$ (Schultz 1992b, c). The increased inhibition of ejecta curtain development uprange due to an atmosphere can cause the final crater to appear elongated perpendicular to the impact direction for $\sim 10° < \Theta < \sim 20°$. Topographic profiles of experimental impacts in the presence of an atmosphere at different impact angles have not been published.

Images of the ejecta curtains in GW78 suggested that most of the observed asymmetries in oblique impact craters involved a general tilting of the ejecta blanket in the downrange direction relative to the vertical impact case. For near-vertical impacts, the ejecta curtain is symmetric around the impact point, with ejection angles of ~45° (Cintala et al. 1999). Recent improvements in imaging techniques have allowed time lapse slices through the ejecta curtain to be imaged, which, in turn, can be converted to particle velocity vectors (Anderson et al. 2000; Schultz et al. 2000). Oblique impact experiments imaged with these new techniques show that the ejecta curtain for oblique impact becomes more symmetric with time due to near-field versus far-field effects (Anderson et al. 2000).

Observations on the terrestrial planets have been largely anectdotal and focused on the morphology rather than the topography of oblique impact craters. GW78 observed many structures on the Moon, Mercury, and Mars that mimicked the appearance of oblique impact structures in the laboratory, and the saddle-shaped topography of Messier was noted by Schultz (1976) as indicative of oblique impact. Comparison of venusian impact craters with experimental craters produced in a dense atmosphere led to a general cataloging of crater shape, central structure appearance, and ejecta distribution for different impact angles (Fig. 42 of Schultz 1992c). Ejecta blankets on Venus were observed with patterns ranging from minor asymmetries to the fly-wing pattern. "Run-out" flows in the ejecta were found to be concentrated in the presumed downrange direction. Rim shapes corresponding to appropriate ejecta patterns were observed: the crater planform was elongated along the projectile flight direction for presumed low impact angles, and slightly higher impact angles showed the planform slightly elongated in the direction perpendicular to flight. Examples were shown indicating that central peak diameters are larger for higly oblique impacts, central structures are offset in the uprange direction, and peak rings have missing sectors in the downrange direction. However, Ekholm and Melosh (2001) measured central structure offset relative to projectile direction of travel and found no evidence for a central structure offset in the uprange direction. Ekholm and Melosh (2001) also found no correlation of central peak diameter to crater diameter for oblique impacts on Venus.

A few surveys have been made of the lowest angle, “grazing impacts” on the terrestrial planets. Schultz and Lutz-Garihan (1982) searched for highly oblique impacts on Mars with diameters >3 km. They looked for craters with an elongate planform, saddle-shaped appearance, butterfly ejecta pattern, and median floor ridge. They listed five categories of features based on degradation state, and they published the location, diameter, and degradation state for those features. Based on comparison with the GW78 experiments, Schultz and Lutz-Garihan (1982) considered these grazing impacts to have occured at $\Theta < 5°$. They found an excess of craters with these low angle effects relative to that expected from Equation 1, and they interpreted that as being due to a population of grazing impactors caused by the orbital decay of captured asteroids (moonlets). They further found that the predominate compass direction of the semimajor axis varied over martian history, and they interpreted this as indicative of true polar wander. However, Bottke et al. (2000) recently surveyed the crater populations on Venus, the Moon, and Mars and found ~5% of the craters on all 3 bodies were highly elliptical. They concluded that the impact angle at which craters become elliptical on the terrestrial planets is higher than in the GW78 experiments into pumice dust, and based on their new surveys of Venus and the Moon, no excess of grazing impacts existed on Mars. They believed that elliptical craters were formed at higher impact angles on the planets because the ratio between crater and projectile diameter was lower than that observed in the laboratory shot experiments of GW78.

In this work, we attempt to empirically determine variation in morphology and shape with impact angle for craters on an airless body, the Moon, and a body with a dense atmosphere, Venus. We survey the crater populations and attempt to determine a logical progression of morphologies corresponding to decreasing impact angle. The percentages of craters with each morphology can be combined with Equation 1 to infer the impact angles at which each morphology occurs. Using topography derived from stereo imagery, we can characterize how the shape of impact craters on Venus and the Moon vary with impact angle.

EMPIRICAL DETERMINATION OF CRATER MORPHOLOGY VERSUS IMPACT ANGLE

Approach

For a planetary surface, the percentage of impactors striking a surface below a given impact angle should be governed by Equation 1, and, therefore, a randomly selected population of impact craters should have predictable percentages formed at different ranges of impact angle. If all other variables that could affect crater morphology were held constant, a survey of a planet’s crater population would be invertible to determine the impact angles for which different crater morphologies occur. Such an ideal situation does not exist, but we believe that we can design surveys of the lunar and venusian crater populations that sufficiently isolate the effects of impact angle on crater morphology. Our approach is to divide the craters into different morphological classes that appear to show progression from a near-vertical to a near-horizontal impact angle. We then count the percentages of fresh craters above a certain diameter that fall within each morphological class. We assume that the experimental and theoretical work provide an approximate guide to what occurs on the planet. For example, we consider increasing asymmetry of ejecta and rim planform to indicate a more oblique impact angle, but the nature of the asymmetry may differ from the experimental work. We desire to have imagery of consistent resolution and viewing conditions that clearly show crater and ejecta morphology for large numbers (hundreds) of craters on a flat, invarying target terrain. Such a data set, unfortunately, does not exist for either planet. For Venus, the primary problem is that not many craters exist on the planet. For the Moon, the problem is observational; typically, distinguishing an impact crater’s ejecta blanket from the underlying terrain is difficult. However, we were able to gather data for enough craters, on the order of a hundred, on each of the planets to draw some meaningful conclusions.

Lunar Data

For the Moon, the Lunar Orbiter and Apollo imagery archives have provided many examples of impact craters that appear to have formed from nonvertical impacts (GW78; Schultz 1976). Of the Apollo era imagery, the Lunar Orbiter high-resolution imagery is probably the best in terms of providing wide-spread coverage at a consistent resolution and viewing angle. However, in that data, only a very small percentage of the craters have ejecta blankets that contrast significantly in albedo with the underlying terrain. Apollo missions 15 through 17 collected stereo imagery from which high-resolution topographic maps were generated. These topographic data are useful for a survey because ejecta blankets retain a topographic signature long after space weathering and gardening have made them indistinguishable in imagery. The topographic data were published as a set of contour maps called the Lunar Topographic Orthophotomaps (LTO) that have a horizontal resolution of about 100 m and contour interval of 100 m. Figure 1 shows the coverage of the LTO data.

We surveyed only craters >5 km in diameter in the LTO sheets that were located on the mare or smooth highlands. These restrictions ensured that we avoided using secondaries in the survey, that the rim topography was resolvable, and that target properties were consistent. We reviewed the LTO sheets to find craters with enough preserved rim topography (a few hundred meters) that we felt we could distinguish any significant asymmetry in the rim topography associated with the impact event. We measured the major and minor axes of the rim of suitable craters. We noted any topographic asymmetry of the rim; the contour interval of 100 m is the minimum rim variation we could observe. For those craters that were fresh enough and located on a smooth enough surface that substantial ejecta topography existed away from the rim, we documented the topographic planform of the ejecta blanket.

We found 91 craters on smooth terrain with rims well enough preserved that we felt confident in evaluating rim topography. The proximity and orientation of Messier and Messier A, along with comparison to experimental results, (GW78) suggest that these craters represent a single impact event. So, the 91 craters represent 90 independent impact events. Fifty-six of the craters had sufficient topography for evaluation of the ejecta planform. Five craters, including both Messier and Messier A, had planforms with ellipticities (major axis/minor axis) >1.2. This represents 4.4% of the independent impact events, a result consistent with the findings of Bottke et al. (2000).

Our 4 classifications for rim topography are symmetric, depressed in a single direction, saddle-shaped, and otherwise irregular. The symmetric classification indicates no measurable variation in rim elevation but not necessarily a circular rim planform. 71 craters have symmetric rims, and all of them have either no ejecta topography or an axially symmetric ejecta distribution. Four of these craters have some measurable noncircularity of the rim, but the ellipticity is <1.1 in all cases.

20 craters have a rim with varying elevation or unevenly distributed ejecta (Table 1). Seven of the 20 are classified as having a single rim depression. Six of those 7 have measurable ejecta topography, and in all cases, the ejecta are concentrated to the opposite side from the rim depression. These craters are consistent with experimental results that show the rim lowered in the uprange direction and ejecta concentrated in the downrange direction for impact angles below 30° (GW78). Four of the craters with a single rim depression have planforms that appear to be elongated slightly in the downrange direction, but the ellipticity is always <1.1.

Seven craters had rim topography that could best be described as saddle-shaped, with rims depressed on opposing sides. Three of the 7 have ellipticities >1.4, with the low points of the rim corresponding to the major axis. Three of the 7 have some topographic expression of the ejecta blanket. The crater Messier, which has an ellipticity of 1.7, has the ejecta entirely concentrated adjacent to the high portions of the rim. The craters Dawes and Greaves have ellipticities <1.1, with

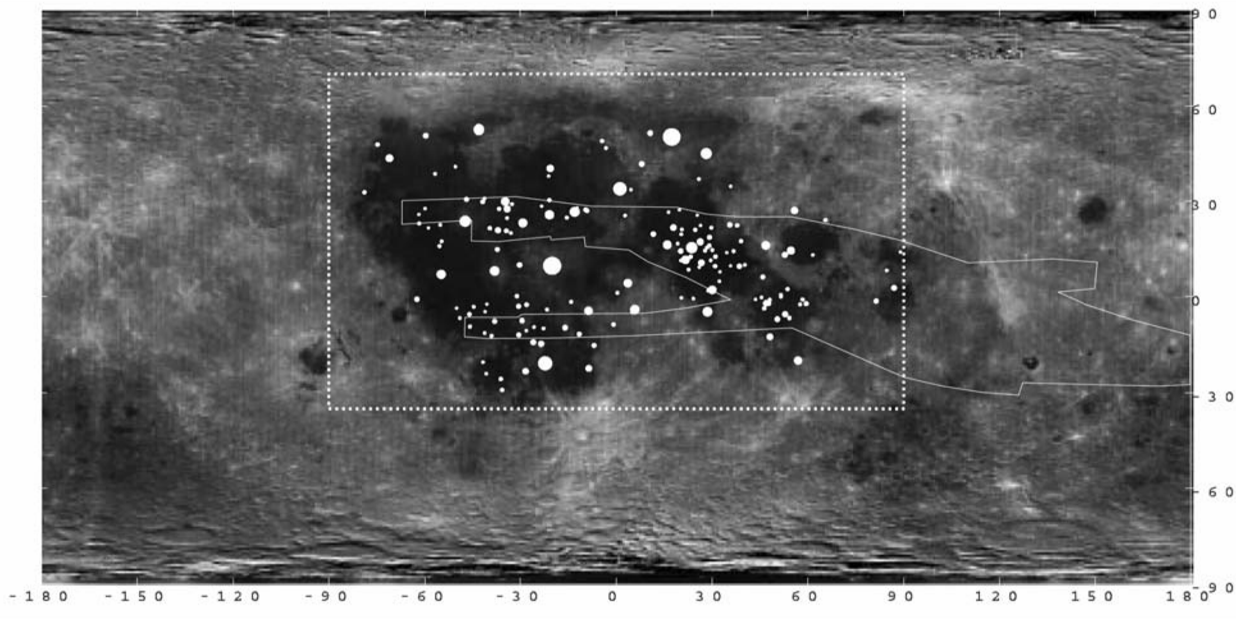

Fig. 1. Clementine albedo map showing LTO coverage (solid outline) and the portion of the Clementine data used in our surveys (dotted line). Impact craters used in the surveys are shown as white circles.

Table 1. List of craters on Lunar Topographic Orthophotomaps with nonsymmetric rims.

Name	Latitude	Longitude	D along Projectile Direction	D across Projectile Direction	Ellipticity	Rim asymmetry[a]	Ejecta asymmetry[b]	Comments
Dawes	17.20°	26.33°	18.3 km	16.8 km	1.09	v	a	
Messier	−0.13	47.67	14.5	8.7	1.67	v	a	
Greaves	13.17	52.78	14.5	13.5	1.07	v	a	
Arago E	8.50	22.70	6.3	4.3	1.47	v	x	
Torricelli	−3.32	28.58	31.5	21.8	1.44	v	x	
Messier B	0.90	48.05	7.0	7.0	1.00	v	x	
Very	25.60	25.37	5.0	5.0	1.00	v	x	
Bessel	21.72	17.92	16.0	15.3	1.05	d	a	
Ross B	11.37	20.30	6.3	6.3	1.00	d	a	
Ross	11.63	21.72	25.5	24.3	1.05	d	a	
Cauchy	9.55	38.62	11.8	12.3	0.96	d	a	
Brayley B	20.72	325.68	9.5	9.5	1.00	d	a	
Lambert	25.75	339.00	30.0	29.2	1.03	d	a	
Beer	27.08	350.87	9.5	8.7	1.09	d	x	
Wollaston	30.58	−47.00	9.8	9.8	1.00	i	s	Review of stereo images suggests LTO incorrect.
Messier D	−2.37	46.33	8.3	7.5	1.11	i	s	Rreview of stereo images suggests LTO incorrect.
Maskelyne	2.17	30.08	25.0	20.0	1.25	i	s	Irregular rim topography due to collapse?
Peek	2.77	86.95	13.5	12.5	1.08	i	a	Elongated perpendicular to projectile direction?
Delisle	29.92	−34.67	25.8	24.8	1.04	i	s	Irregular rim topography due to collapse?
Messier A	−1.97	46.95	15.8	11.0	1.44	i	a	Shallow and elongated downrange, ricochet from Messier?, ejecta almost all downrange.

[a]V-shaped (v), depressed rim (d), in uprange direction, or irregular (i).
[b]Asymmetric (a), symmetric (s), or not preserved (x).

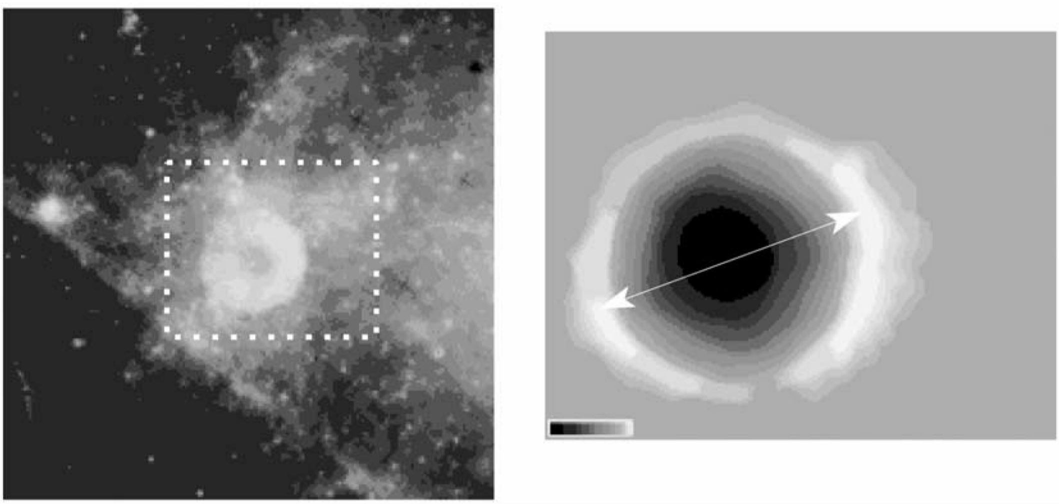

Fig. 2. Apollo 16 metric camera image of Peek crater (left) and digitized LTO topography (right). The arrows indicate the long axis of the impact crater. The scale bar is 4 km and spans elevations of 1.7 to 4.3 km.

the major axis in line with the the rim low points. Their near-rim ejecta are concentrated adjacent to the rim highs, but more distal ejecta contours become more circular. Examples of craters with a single rim depression and saddle-shaped topography are shown and discussed in more detail in the section on lunar crater topography.

Six craters have rim and ejecta topography that are unusual in some way. Peek (Fig. 2) has rim topography similar to the saddle-shaped craters, with opposing lows; however, the lows are not at equal elevations and are aligned with the minor axis of the crater. For some of their experimental impacts into pumice with pyrex projectiles at angles between 10° and 30°, GW78 noted an elongation of the crater perpendicular to the projectile direction, and Peek may represent an example of this. Alternatively, Peek is located in a region where Mare Smythii should be thin and the unusual

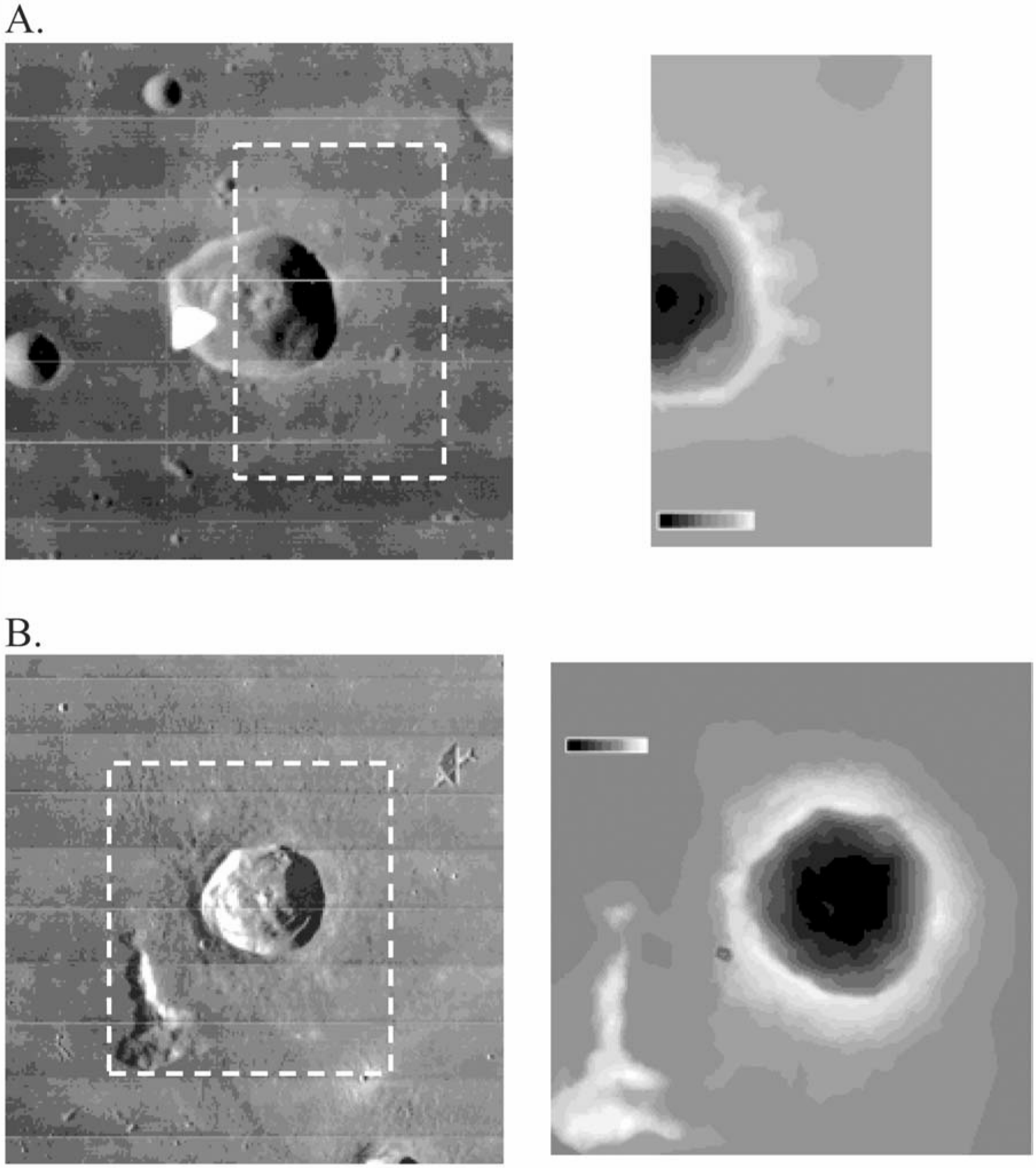

Fig. 3. Lunar Orbiter images (left) and digitized LTO topography (right) for (a) Maskelyne and (b) Delisle. The scale bars are 10 km and span elevations of 3.3 to 6.6 km for Maskelyne and 3.4 to 6.6 km for Delisle. These craters have symmetric ejecta blankets with irregular rim structures that we attribute to crater collapse processes.

topography may represent structural control of ejecta emplacement. Maskelyne and Delisle (Fig. 3) have irregularities in rim planform and topography but their ejecta blankets have symmetric topography; we conclude that rim irregularities in these craters are related to complex crater collapse. Wollaston (Fig. 4) shows some asymmetry in the rim and ejecta contours in the LTO sheets. However, the crater appears symmetric in the Apollo stereo imagery, but the images in this area have a low sun angle. We believe the asymmetry in Wollaston's topography represents a minor error in the production of the LTO resulting from the difficulty of using low sun angle images for photogrammetry. Similarly, a review of the stereo imagery for Messier D (Fig. 4) suggests that the LTO for this crater is inaccurate. Messier A appears to have resulted from a ricochet downrange from Messier, the original point of impact. We

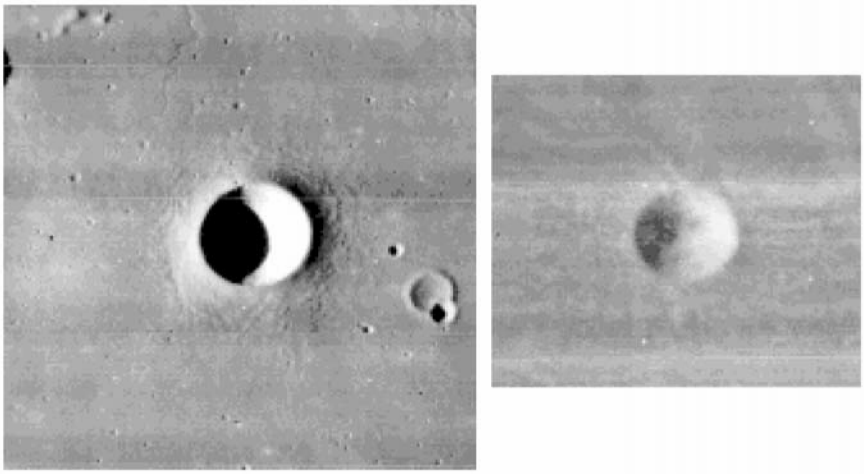

Fig. 4. Lunar Orbiter images of Wollaston (left, 9.8 km diameter) and Messier D (right, 8.3 km diameter). Both craters appear to be topographically axisymmetric.

Table 2. Percentages of lunar craters with different characteristics in the LTO data.

Category	Count[a]	Cumulative fraction[b]	90% CI[c]	$\sin^2\Theta$[d]	$\sin^3\Theta$[e]	Predicted Θ[f]
Elliptical rim	4	0.044	0.036	5–16	12–26	5
Nonelliptical rim	86	1.000	–	–	–	–
Total	90					
Saddle-shaped	7	0.079	0.047	10–21	19–30	5
Depressed side	7	0.157	0.069	17–28	26–38	30
Symmetric	75	1.000	–	–	–	–
Total	89					
Butterfly ejecta	3	0.056	0.052	4–19	9–28	5
Asymmetric	7	0.185	0.087	18–31	27–40	30
Symmetric	44	1.000	–	–	–	–
Total	541					

[a]Messier and Messier A counted as a single impact.
[b]Cumulative fraction of the total number of craters.
[c]90% confidence interval for cumulative fraction.
[d]Using a 90% confidence interval, onset angle assuming cumulative fraction equals $\sin^2\Theta$
[e]Using a 90% confidence interval, onset angle assuming cumulative fraction equals $\sin^3\Theta$.
[f]Predicted onset angle from experimental work of GW78.

discuss Messier and Messier A in more detail in the section on oblique impact topography.

Table 2 summarizes the results from the LTO data in terms of a cumulative percentage of craters and estimated impact angle. In accordance with experimental impacts into noncohesive targets in a vacuum (GW78), the progression observable in the topographic data, with decreasing impact angle, is: 1) the impacts that are most near-vertical have axisymmetric rims and ejecta blankets, and the rim has a constant elevation; 2) with decreasing impact angle, the rim becomes depressed uprange and ejecta becomes concentrated downrange, opposite the depressed rim; 3) as the impact angle decreases, the rim topography becomes saddle-shaped, with ejecta concentrated in the crossrange direction; and 4) the crater becomes highly elongated in the downrange direction. For comparison, we show the approximate impact angles at which these phenomena occur in the experimental work (GW78).

The fifth column of Table 2 shows the impact angle based on the formula:

$$\Theta = \arcsin(P^{1/2}) \tag{2}$$

where P is the cumulative fraction of craters. Equation 2 is the integral of Equation 1 inverted to solve for the impact angle. Use of Equation 2 assumes that the percentage of impact craters above a particular diameter equals the percentage of impactors striking the planet at different angles. However, if final crater diameter is dependent on impact angle, using a minimum crater diameter threshold makes this assumption invalid. Experimental work (GW78) suggests that the vertical component of velocity, or $v\sin\Theta$, determines final crater diameter. Craters several km in diameter on the terrestrial planets should form in the gravity regime, so the appropriate scaling relationship (e.g., Schmidt 1980) suggests approximately a $\sin\Theta$ dependence of displaced mass on impact angle. This means that an impactor striking at 10° from horizontal would need to be a factor of 5 larger in diameter to produce the same size crater as a near-vertical impactor. In other words, setting a minimum crater diameter for counting purposes creates the likelihood that craters formed from small, near-vertical impactors will be counted but those from similar-sized oblique impacts will not be. This effect can be accounted for if the size distribution of impacting objects is assumed to have a simple negative exponential dependence and cratering efficiency is assumed to have a $\sin\Theta$ dependence on impact angle.

The percentages of impact craters attributable to different impact angles can be estimated following the procedure outlined in GW78. As discussed in detail below, experimental and observational evidence suggests that the depth-diameter ratio does not change significantly with impact angle. If proportional growth for the transient cavity is assumed, then, to first order:

$$D^3(\Theta) = D_{90}^3 \sin\Theta \tag{3}$$

where $D(\Theta)$ is the transient-crater diameter at angle Θ, and D_{90} is the diameter at vertical incidence. Typical scaling laws have the final crater diameter as a simple exponential dependence on impactor mass (e.g., Melosh 1989), or

$$D_{90} \propto m^{\beta} \tag{4}$$

If α is used to represent the exponential mass distribution of impactors expected for the terrestrial planets (GW78), Equation 1 can be translated into

$$dN(m, \Theta) \propto m^{\alpha}\cos\Theta\sin\Theta d\Theta \tag{5}$$

where dN is the differential number of objects with masses equal to or greater than m that will impact with a trajectory angle Θ (GW78). Substituting Equation 3 and Equation 4 into Equation 5 yields:

$$dN(D, \Theta) \propto D^{\alpha/\beta}\cos\Theta\sin\Theta^{(1-\alpha/3\beta)}d\Theta \tag{6}$$

where dN is now the differential number of craters above diameter D. If we use $\beta = 0.26$ and $\alpha = -0.8$ so that $\alpha/\beta \cong -3$ (e.g., McKinnon et al. 1997), Equation 6 simplifies to:

$$dN(D, \Theta) \sim\propto D^{-3}\cos\Theta\sin^2\Theta d\Theta \tag{7}$$

In other words, to a first approximation, the percentage of objects striking the surface below a given angle Θ should be $\sin^2\Theta$, but the percentage of impact craters above a diameter D that result from those impacts should be $\sin^3\Theta$. In Table 2, we show the estimated impact angles that would occur for both a $\sin^2\Theta$ distribution (column 5; no crater size dependence on impact angle) and the $\sin^3\Theta$ distribution (column 6). The angles in Table 2 are shown as a range based on an estimate of the 90% confidence interval for the fraction of craters in each classification (Johnson 1973).

By definition, our survey of the LTO data uses the portions of the ejecta blanket that have significant topography. However, in the experimental work of GW78 and the anecdotal examples they show, the distal portions of the ejecta blanket primarily define the overall appearance of the ejecta blanket, and these distal portions have a negligible topographic signature. A survey using imagery rather than topography provides a direct comparison with images of the ejecta distribution around experimental impact craters (GW78). As mentioned above, the ejecta blankets are clearly defined in only a very small percentage of the craters in the Lunar Orbiter imagery.

The Clementine mission produced global imagery in several spectral bands at ~200 m resolution (Nozette et al. 1994). We chose to use the data from the UV/VIS camera collected with 750 nm filter. The global mosaiced version of this data is often referred to as the Clementine "albedo map." The dynamic range of these data is superior to that of the Lunar Orbiter photographs, and the digital format allows image enhancement techniques to be used to highlight albedo differences attributable to ejecta blankets. In certain geologic settings (e.g., near highland-mare contacts), color ratios of the Clementine multi-spectral data may make ejecta blanket identification easier, but in the interests of simplicity and consistency, we chose to use only the 750 nm data.

Our survey area covered the terrain between 35°S to 70°N on the nearside of the Moon. This area encompasses the majority of the lunar maria. We conducted a preliminary survey by describing asymmetric ejecta blankets for craters more than 2 km in diameter over a limited area. We found that the ejecta patterns fell into 4 classes illustrated in Fig. 5. These can be described, in order of decreasing impact angle, as 1) symmetric; 2) generally circular with the ejecta offset, presumably downrange, relative to the crater center; 3) a sector of ejecta missing, presumably uprange; and 4) butterfly ejecta pattern. For craters from 2–5 km in diameter and craters in the mare, identifying an asymmetric ejecta blanket was relatively easy, but distinguishing the nature of the asymmetry was difficult. For the full survey, we classified mare craters over 5 km in diameter with well-defined ejecta blankets. In general, these correspond to Copernican and Eratosthenian craters.

We found 86 craters suitable for classification in our study area. Their locations and classifications are shown in Fig. 6, and the data are summarized in Table 3. Slightly less than half of the craters have ejecta that are asymmetric in some way. A forbidden zone exists uprange for 29% of the craters, and the ejecta show a butterfly pattern for 5% of the craters.

Some overlap occurs between the LTO and Clementine surveys, and 12 impact craters (counting Messier and Messier A as a single impact) appear on both surveys. Comparison of the shapes and distal ejecta planforms of experimental impacts into pumice in GW78 indicates that craters with symmetric distal ejecta should have symmetric rim shapes,

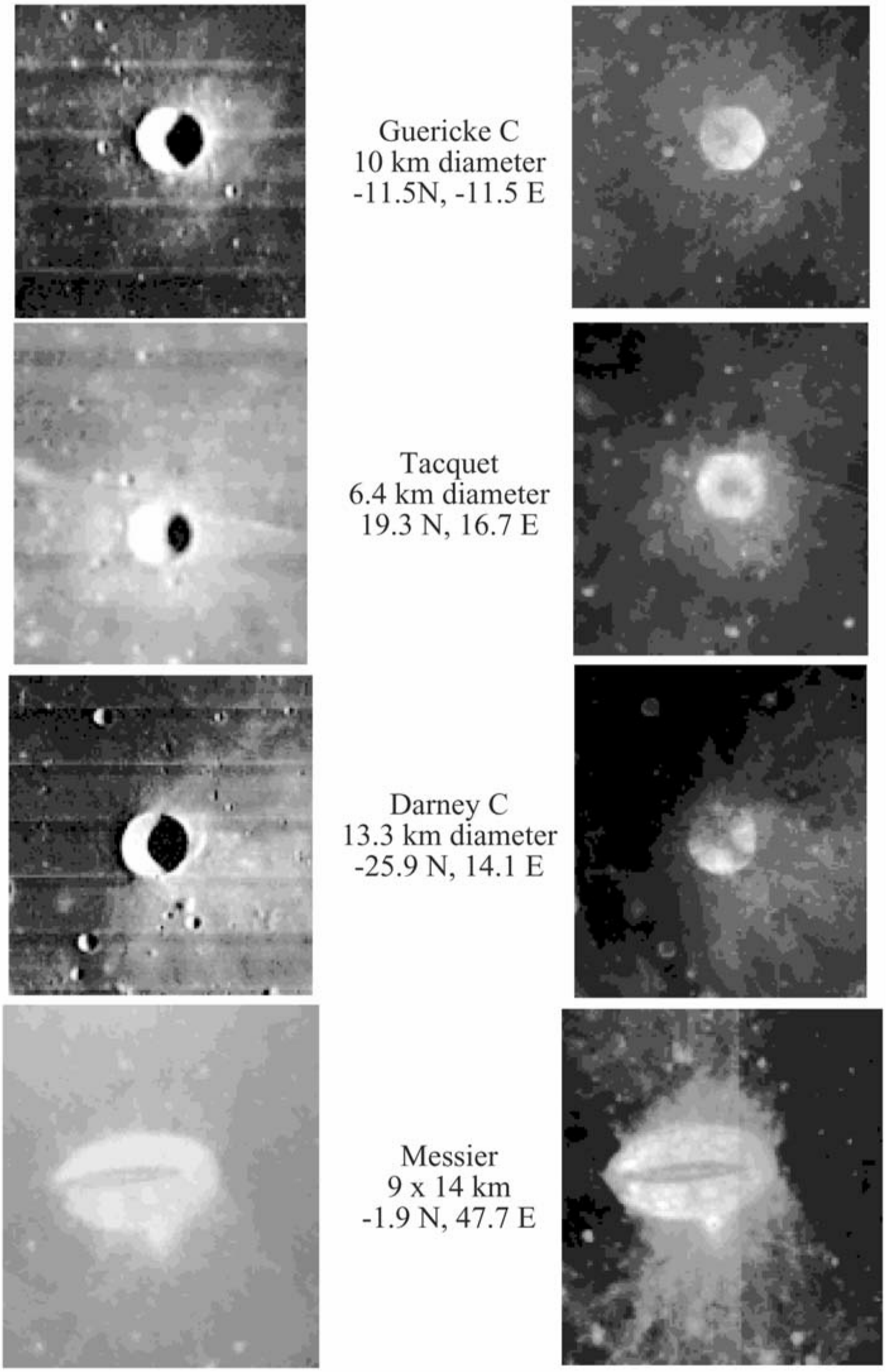

Fig. 5. From top to bottom, examples of lunar impact craters with ejecta distributions indicating increasingly horizontal impact angles. The left images are from Lunar Orbiter, and the right images are from the Clementine data. As the impact angle becomes more oblique, the ejecta become offset downrange, a forbidden zone develops uprange, and finally, a butterfly ejecta pattern is observed.

craters with butterfly distal ejecta should have saddle-shaped rims, and craters with a clear forbidden zone in the distal ejecta pattern should have a depressed rim in the uprange direction. The transition in the experimental work toward a depressed uprange rim appears to occur at a higher impact angle than development of a complete forbidden zone in the distal ejecta. Thus, the experimental data suggest that some craters with asymmetric ejecta (but not a forbidden zone) will have symmetric rims, and some will have a depressed uprange rim. However, Tables 2 and 3 suggest that a forbidden zone in the distal ejecta forms at a higher impact angle than a depressed uprange rim.

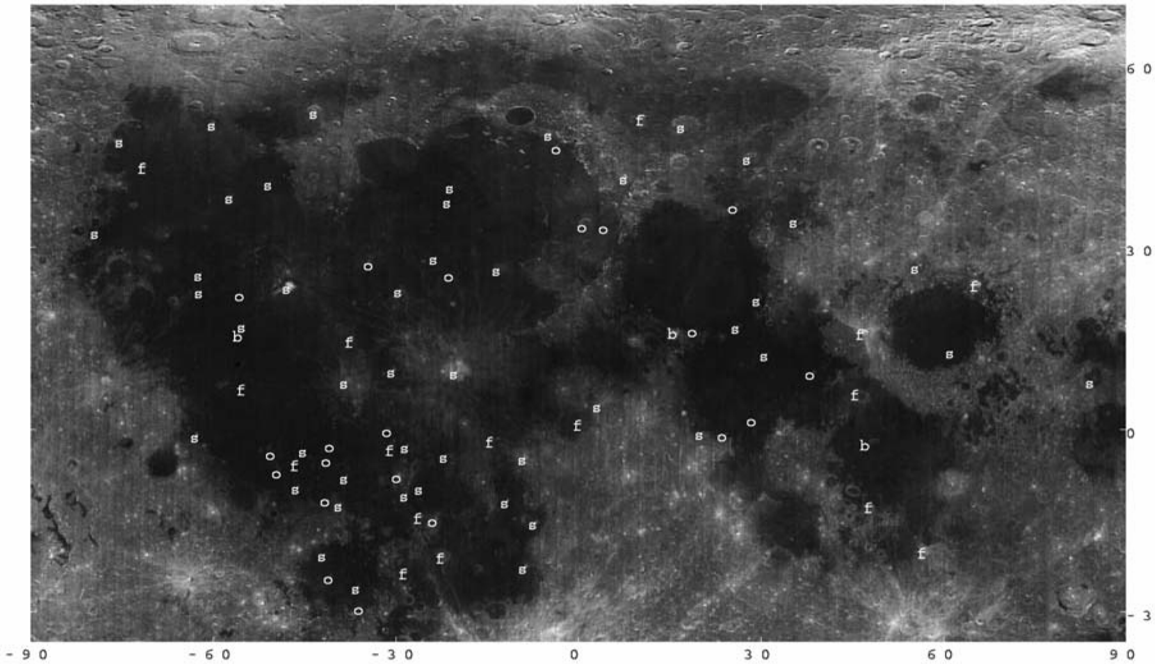

Fig. 6. Location and classification of lunar impact craters surveyed with the Clementine 750 nm global mosaic. The ejecta blankets for craters >5 km in diameter are classified as symmetric (s), offset (o), forbidden (f) zone, and butterfly (b) pattern.

Table 3. Percentages of lunar craters with different ejecta patterns in Clementine data.[a]

Category	Count	Cumulative fraction	90% CI	$\sin^2\Theta$	$\sin^3\Theta$	Predicted Θ
Butterfly	3	0.035	0.033	3–15	8–24	5
Forbidden	16	0.221	0.074	23–33	32–42	20
Offset	21	0.465	0.089	38–48	46–55	45
Symmetric	46	1.000	–	–	–	–
Total	86					

[a]Descriptions of columns as in Table 2.

Two of the craters in both surveys clearly do not have rim topography and ejecta patterns in the Clementine data that match expectations from the experimental work. The distal ejecta for Peek shows a forbidden zone to the ESE, but the low axis of the rim topography is NNW-SSE, while the WNW-ENE axis is elongated. The ejecta distribution in Clementine data for Dawes appears symmetric, but the north rim is depressed. Both of the craters occur in areas where the maria are likely to be thin (Peek is in Mare Smythii, and Dawes is in Mare Tranquilitatis near the border with Mare Serenitatis), and some unknown subsurface structure may affect rim shape.

The 10 remaining craters are consistent with what would be predicted from the experimental results. Two of the craters, Cauchy and Lambert, have uprange depressed rims and clearly have some ejecta in the uprange direction in the Clementine data. Near-rim contours in the LTO data for Cauchy and Lambert show some ejecta in the uprange direction and are also consistent with the idea that a depressed rim occurs at higher angles than a forbidden zone in the ejecta blanket. In summary, individual craters that fall within both surveys appear as expected based on the experimental work of GW78, but the overall surveys indicate that a forbidden zone develops at a higher impact angle than a depression in the uprange rim. This discrepancy arises primarily because the percentage of craters in the Clementine survey with a forbidden zone in the distal ejecta is higher than predicted by the experimental work. In the surveys of lunar data that we conducted, the most difficult and subjective task was distinguishing, in the Clementine imagery, between craters with distal ejecta that were merely asymmetric and those that had a forbidden zone. Perhaps, a process such as space weathering causes the distal ejecta signature to be reduced without being removed, and less ejecta uprange appear to become no ejecta uprange. Figure 7 shows a rough schematic of the progression in shape and ejecta blanket appearance with decreasing impact angle for lunar craters.

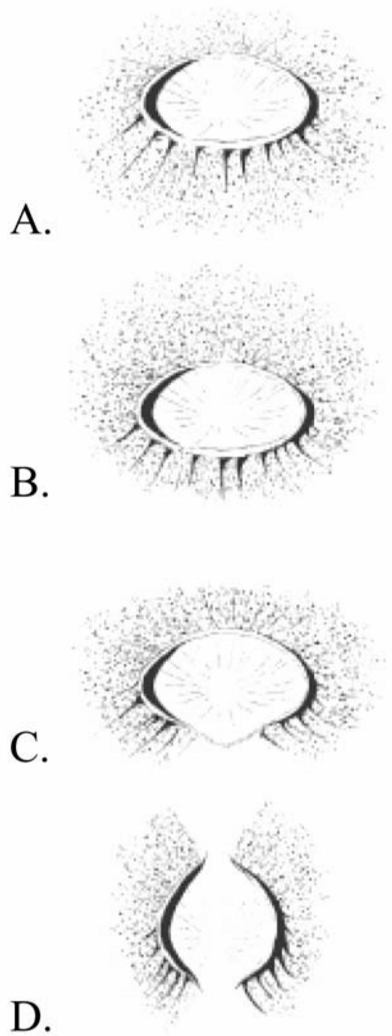

Fig. 7. Rough sketches of the progression of crater topography and ejecta pattern with decreasing impact angle. The impact angle becomes more horizontal from top to bottom, and the bottom of the page is the uprange direction in all cases: a) for near-vertical impacts, both the rim and ejecta blanket are axisymmetric; b) as the impact angle decreases, ejecta begin to be offset in the downrange direction; c) with further decrease in the impact angle, a forbidden zone develops uprange and the uprange rim becomes depressed; d) for the lowest angle impacts, both the uprange and downrange rims are depressed, the crater may be elliptical, and ejecta are concentrated in the crossrange directions.

Venusian Data

Venusian ejecta blankets are relatively easy to identify in Magellan Synthetic Aperture Radar (SAR) data. At the radar wavelength of 12.6 cm, the ejecta are typically rough relative to the surrounding plains. The ejecta appear to be emplaced primarily as flows (Phillips et al. 1991; Herrick and Phillips 1994), so the ejecta blanket boundaries are well-defined. The dense atmosphere on Venus causes meteoroids to be disrupted in the atmosphere so that the smallest impact crater on Venus is a few km in diameter. The longer path length causes meteoroids entering the atmosphere at low angles to be preferentially filtered out, and the size-frequency distribution of craters may be deficient in low-angle impacts up to 20–30 km in diameter (Tauber and Kirk 1976; Ivanov et al. 1986; Ivanov 1990; Herrick and Phillips 1994). Therefore, we surveyed only craters >30 km in diameter.

Recent work has suggested that all craters with radar-dark backscatter properties in their floor have experienced post-impact volcanic infilling and embayment (Sharpton 1994; Herrick and Sharpton 2000). However, for most craters, enough of the ejecta blanket appears to remain for the original planform of the ejecta to be characterized. We surveyed all craters over 30 km in diameter that appeared to have enough ejecta remaining to determine their ejecta planform, but we separately tracked those craters with radar-bright floors.

We characterized the ejecta planforms in a manner consistent with Schultz (1992c). Figure 8 shows examples of the 5 different classifications. The classes are: 1) ejecta planform symmetric or nearly symmetric around the crater rim; 2) ejecta planform offset in a particular direction, but ejecta entirely surrounding the rim; 3) ejecta planform has a notch in it that reaches the rim; 4) planform shows a sector of the rim lacking ejecta; and 5) the rim is elliptical and the planform has a "fly-wing" pattern swept downrange. We were able to categorize 120 craters, 26 of which had radar-bright floors. Table 4 summarizes the results. In general, the results for all the craters are consistent with those for bright-floored craters only, and this suggests that using the larger data set for statistical analysis is valid. A possible exception is that modest embayment may cause craters with an offset ejecta blanket to appear to have ejecta missing up to the rim, and this could account for the higher percentage of the former relative to the latter for the bright-floored craters.

Discussion

Although the error bars are large, particularly at the lowest impact angles, the data are mostly consistent with predictions from experimental and theoretical work. The observed ejecta planforms, and the percentages of craters with those planforms, match well with the experimental observations of GW78 and Schultz (1992c). In general, a $\sin^2\Theta$ dependence for cumulative fraction seems to give impact angles that match experimental predictions better than a $\sin^3\Theta$ dependence. The results provide no compelling evidence that cratering efficiency for planetary impacts is strongly dependent on impact angle. Comparison of the Clementine data with the LTO data shows that, for lunar craters, the distal ejecta becomes asymmetric at much higher impact angles than significant asymmetries in crater topography. These observations are consistent with the ejecta

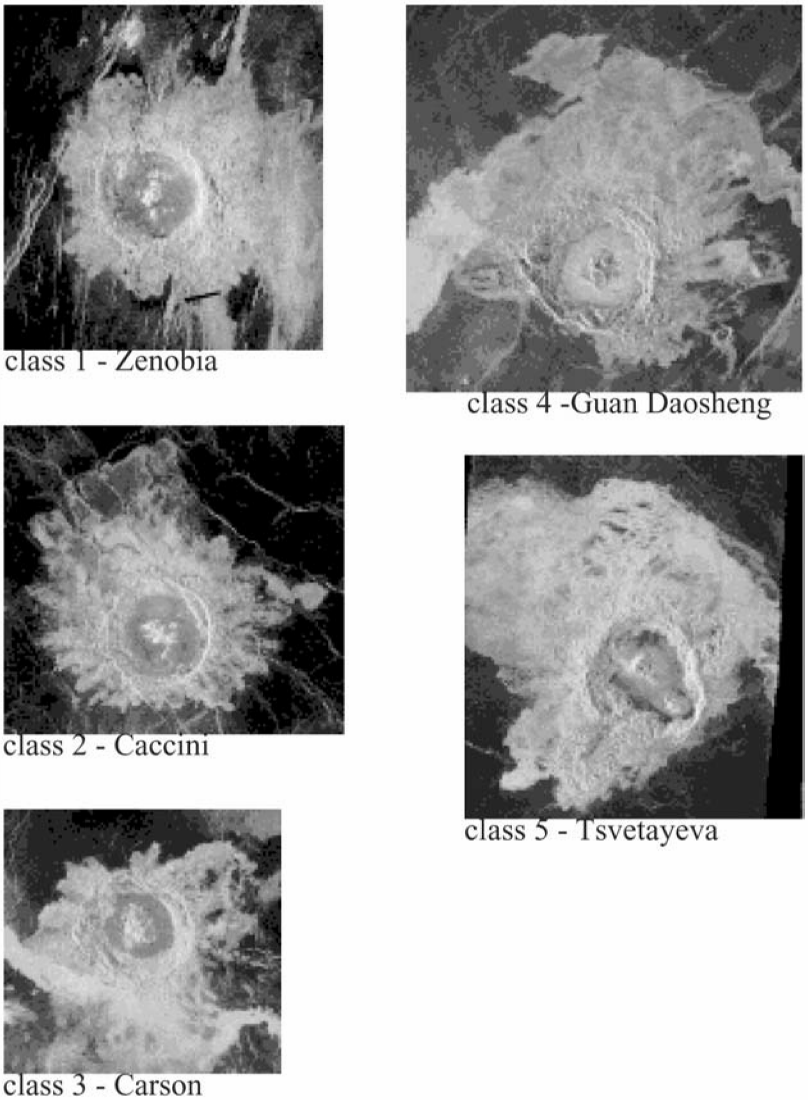

Fig. 8. Venusian craters ~40 km in diameter illustrating the classifications of ejecta blankets and rim planforms indicating increasingly horizontal impact angles. The classes match those specified in Schultz (1992c). As the impact angle becomes more oblique, the ejecta become increasingly offset downrange, and the portion of the rim void of adjacent ejecta increases. Runout flows of ejecta occur predominantly in the downrange direction.

curtain evolving with time from asymmetric to symmetric during an oblique impact event.

Some observations were inconsistent with the experimental work. On the Moon, the percentage of craters with a forbidden zone in the distal ejecta, as observed in the Clementine data, is somewhat higher than expected from the GW78 experiments. This may be due, in part, to differences in observational conditions between the experiments and the Clementine data. In particular, space weathering may make craters with some uprange ejecta appear to have no uprange ejecta. Only one possible example on the Moon, and no examples on Venus, was found of craters elongated perpendicular to the impact direction. Although the statistics are poor, both Venus and the Moon show a higher percentage of the very lowest angle impact craters with an elliptical rim planform, saddle-shaped rim topography, and butterfly or fly-wing ejecta patterns when compared to the experimental results of GW78. This excess is particularly true if an angular dependence exists for crater diameter. For a sinΘ dependence of crater diameter on impact angle, 0.07% of the craters in a specified size range should be the result of impacts occurring at less than 5° from horizontal. Thus, the experimental results of GW78 predict that a sample size of ~100 craters is unlikely to find even a single crater with butterfly ejecta or an elliptical, saddle-shaped rim. Our results are consistent with the more statistically significant survey of Bottke et al. (2000), which found that ~5% of the impact craters on the Moon and Venus have elliptical planforms.

Table 4. Percentages of venusian craters with different ejecta patterns in Magellan data.[a]

Category	Count	Cumulative fraction	90% CI	$\sin^2\Theta$	$\sin^3\Theta$	Predicted Θ
All craters >30 km diameter						
Fly-wing	5	0.042	0.036	4–16	11–25	10
Quadrant missing	17	0.183	0.069	20–30	29–39	20
Notch	31	0.442	0.088	36–47	45–54	30
Offset	30	0.692	0.082	51–62	58–67	50
Symmetric	37	1.000	–	–	–	–
Total	120					
Bright-floored craters >30 km diameter						
Fly-wing	0	–	–	–	–	10
Quadrant missing	4	0.154	0.064	17–28	27–37	20
Notch	3	0.269	0.079	26–36	35–45	0
Offset	9	0.615	0.087	47–57	54–63	50
Symmetric	10	1.000	–	–	–	–
Total	26					

[a]Description of columns as in Table 2.

TOPOGRAPHY OF OBLIQUE IMPACTS

Procedure

In this section, we characterize the topography of impact craters showing the different categories of ejecta and rim planforms discussed in the preceding section. Ideally, we would be able to survey the topography of large numbers of craters in each category and then statistically summarize our observations. Unfortunately, inadequate topographic data coverage exists on either the Moon or Venus to facilitate this desired approach. Given the limited data available, the approach we take is, by necessity, anecdotal. For a few size ranges of craters, we compare and contrast examples of each of the categories identified in the preceding section.

On the Moon, global topographic coverage is provided by the laser altimeter data from the Clementine mission. These data have a horizontal resolution of ~50 km (Zuber et al. 1994), which is inadequate for the purposes of this study. The LTO maps provide excellent horizontal and vertical resolution but, as discussed above, provide data for only a few tens of fresh craters. Clementine stereo data can be used to generate topography with a horizontal resolution on the order of a km (Cook et al. 2000). Imaging angles and coverage are best near the poles, around which a few smooth surfaces occur. We do not use the Clementine stereo data in this work, but when a global DEM is released (Cook et al. 2000), a follow-up study with these data will be performed to check the results presented here.

On Venus, the global radar altimetry data collected by Magellan has a horizontal resolution of ~10 km, a resolution inadequate to characterize rim and ejecta topography for venusian craters. Digital elevation models with a horizontal resolution of ~1 km and vertical resolution of ~100 m can be developed using left-left stereo imagery from Magellan (Herrick and Sharpton 2000). However, stereo coverage exists for only ~20% of the surface, only 168 impact craters. A significant fraction of those craters have only small portions covered in stereo.

Lunar Craters

The depths and rim heights of fresh lunar craters are well-behaved exponential functions of diameter (Pike 1980). In Fig. 9, we show rim-floor depths, terrain-floor depths, and rim heights for the craters with nonsymmetric rims relative to trends calculated by Pike (1980) for all the lunar craters with reliable depth data. Figure 9a shows the depths from the rim to the crater floor as measured by Pike (1980) for all the craters in Table 1. Figure 9a does appear to show a general trend where the craters with asymmetric rims are anomalously shallow. However, when we looked at Pike's rim height data for those craters and compared his measurements to the LTO maps, Pike appears to have used a mean rim elevation in calculating the rim-floor depths. The experimental data of GW78 suggest that interior cross-range profiles should be self-symmetric regardless of impact angle. In other words, if profiles of experimental craters generated by different impact angles are scaled to have the same rim-to-rim diameter, then the profiles are nearly identical. This implies that the depth of oblique impacts relative to the surrounding terrain (or the volume displaced versus diameter) should not vary with impact angle. The maximum rim height for a crater caused by oblique impact should be the same as near-vertical impacts, but the minimum rim height should be much lower.

Figure 9b shows the terrain-floor depths for the craters in Table 1 versus the overall trend from Pike's (1980) data. The terrain-floor data and trend were calculated by subtracting Pike's (1980) rim height data and trend from his rim-floor depth data and trend, respectively. Figure 9c shows the maximum and minimum rim heights that we interpreted from the LTO sheets versus the rim height trend in Pike (1980). With the exception of craters between 10–15 km in diameter, craters with

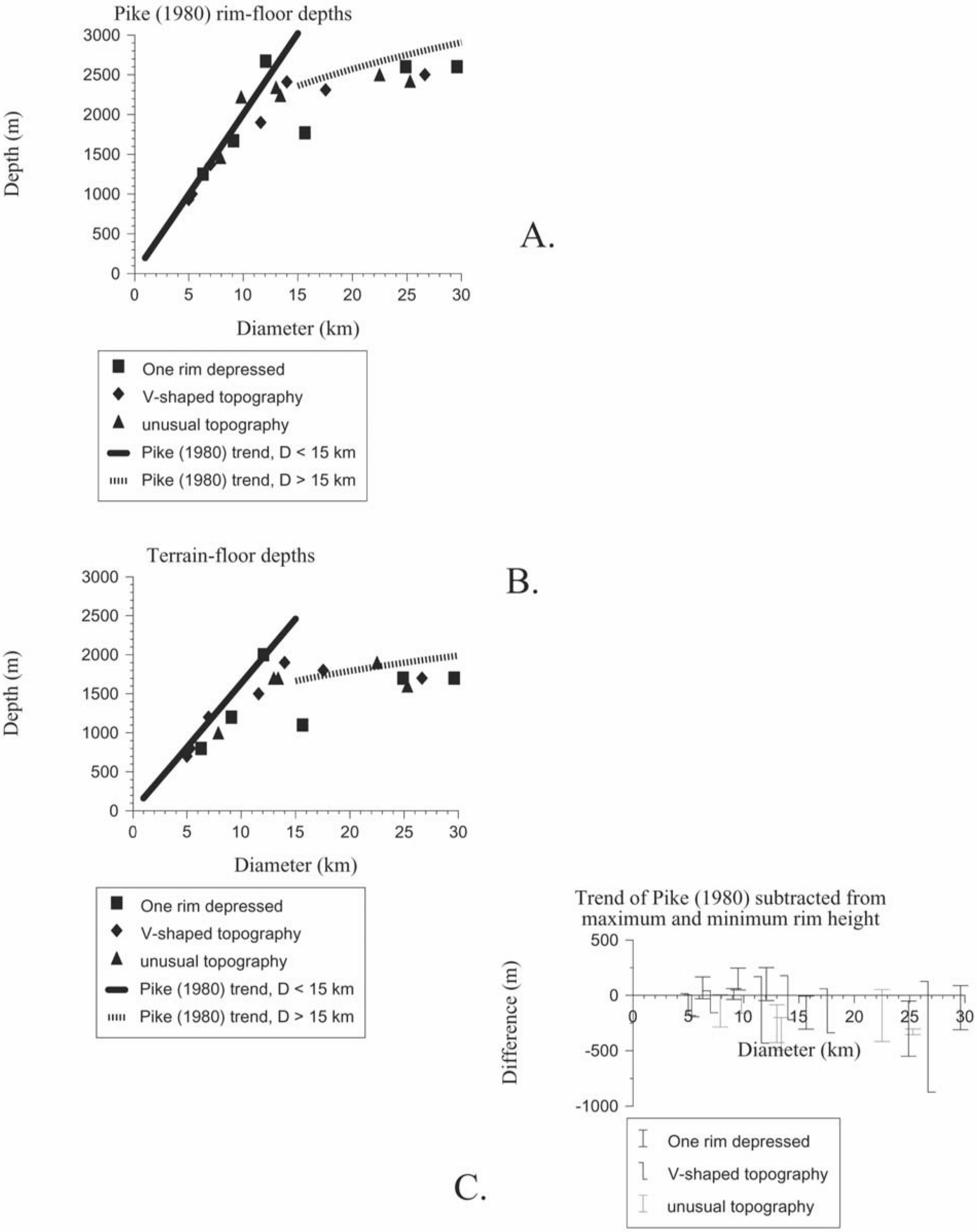

Fig. 9. Comparison of lunar impact craters used in this study with trends from Pike (1980) for fresh lunar impact craters: a) the trend for rim-floor depths subtracted from the rim-floor depth for each crater; b) the trend for terrain-floor depths subtracted from the terrain-floor depth for each crater; c) the trend for rim heights subtracted from the maximum and minimum rim height for each crater as determined in this study.

asymmetric rims do not appear to have unusually low terrain-floor depths. Pike's (1980) data show a wide range in rim-floor depths for the crater population in this diameter range, within which the transition from simple to complex craters occurs. For Figs. 9a and 9b, we used the best-fit rim-floor depth trends for craters below and above 15 km in diameter:

$$d_{rf} = 0.196D^{1.010},\ D < 15\ \text{km}$$

$$d_{rf} = 1.044D^{0.301},\ D > 15\ \text{km} \qquad (8)$$

where d_{rf} is rim-floor depth and D is crater diameter, both in km (Pike 1980). The trend for D <15 km gives a 660 m greater rim-floor depth at a diameter of 15 km than the trend for D >15 km. The crossover point between the two trends, or the diameter where the equations give the same result, is 10.6 km. Figure 10 shows the raw terrain-floor depths for fresh craters of 11–16 km in diameter from Pike (1980). From these data, the oblique impacts (solid symbols) appear to have depths consistent with those of near-vertical impacts (open symbols). The exception is Bessel, which is unusually shallow. Bessel has much more interior slumping than other similar-sized craters, and material has ponded on the floor; the reason for this cannot be determined with existing data.

Rim elevations (Fig. 9c) seem consistent with what is expected from the experimental data. Comparison of our rim height data with the rim-height trend of Pike (1980) indicates that the maximum rim height of an oblique impact is similar to that of a crater with an axisymmetric rim. The low point, however, is substantially lower than the rim of a near-vertical impact of equal diameter. In some cases, the low point of the rim for an oblique impact is at the level of the surrounding terrain.

In Fig. 11, we show imagery and topography for similar-sized craters (10–15 km in diameter) that progress from what we interpret as near-vertical to near-horizontal impacts. The progression from Sulpicius Gallus to Messier in Fig. 11 parallels the GW78 experimental observations. Sulpicius Gallus, a crater interpreted to result from a high-angle impact, is nearly axisymmetric in all aspects. Cauchy has one rim depressed and a lack of distal ejecta in the uprange direction. Interior slopes in Sulpicius Gallus and Cauchy are identical, and the interior of Cauchy is axisymmetric.

The distal ejecta for Greaves can not be distinguished in either Clementine or Lunar Orbiter imagery, so the projectile direction of travel must be inferred from the shape of the crater. Greaves is elongated in the NW-SE direction, and we interpret this as the line along which the projectile traveled. The lowest portion of the rim is to the NW, and we interpret this as the uprange direction. The uprange and downrange rims are substantially lower than the crossrange direction. The interior slopes are identical in the crossrange and downrange direction, and they are the same as for Sulpicius Gallus and Cauchy. In other words, the interior contours are ellipses, and the distance between consecutive contours does not vary along their perimeter. This requires that the floor of Greaves is much more elongated than the rim, as the absolute difference between the major and minor axis is maintained from floor to rim. Excavated material is concentrated in the crossrange direction. While the crossrange rims for Greaves are not higher than those for similar-sized craters with symmetric rims, comparison with Sulpicius Gallus shows that they are wider.

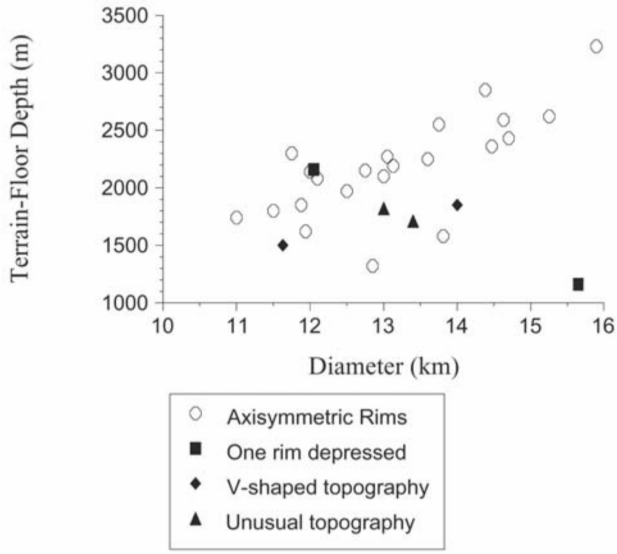

Fig. 10. Terrain-floor depths of impact craters 11–16 km in diameter as measured by Pike (1980). Only one crater that is likely to have resulted from an oblique impact, Bessel, has an unusually low terrain-floor depth.

The easily identifiable distal ejecta pattern indicates that the projectile direction of travel is WSW for Messier and Messier A (Fig 11). Messier completes the sequence of shape variation with decreasing impact angle. Essentially no rim exists in the uprange and downrange direction, and ejecta are entirely concentrated in the crossrange direction. Rim height in the crossrange direction is similar to the other craters in the sequence. In the upper portion of the interior, the walls are of similar slope in all directions and similar in slope to the walls of other craters of similar size. However, within a few hundred meters of the crater floor, the slopes of the uprange and downrange walls decrease, while the crossrange slopes are constant down to the floor. The perimeter to surface area ratio for a highly elliptical crater like Messier is much higher than for circular craters. This means that the rims in the crossrange direction can accomodate the entire ejecta volume and yet are narrower than the rim for Sulpicius Gallus, a circular crater with an axisymmetric rim. A central ridge exists in Messier, which is tens of meters high and runs the length of the floor, which is not visible in the gridded topography because of the kriging algorithm we used.

Messier A is an unusual crater that, while apparently associated with Messier, does not seem to have an analogue in

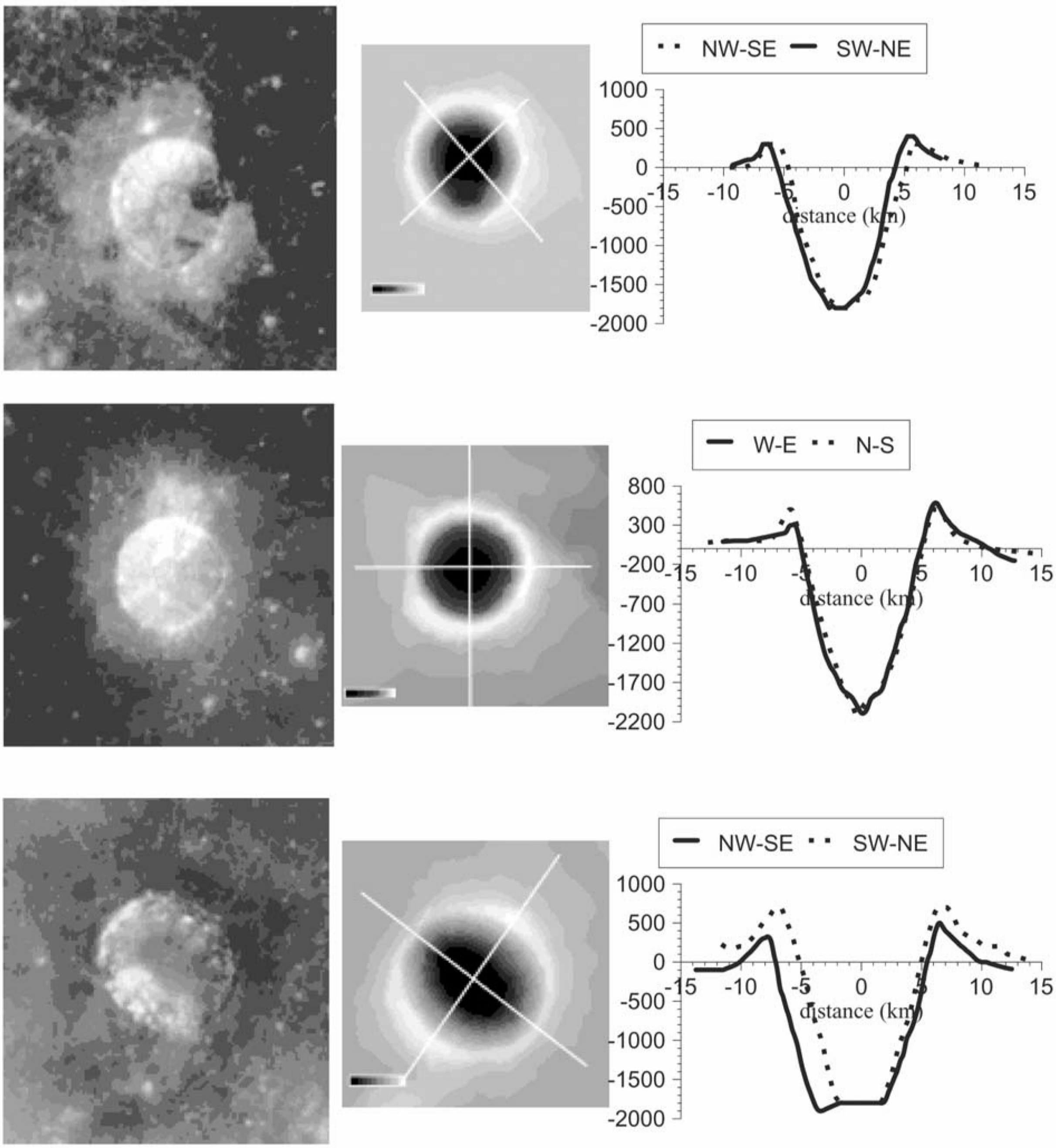

Fig. 11. Clementine imagery, LTO topography, and profiles of lunar impacts 10–15 km in diameter that show the effects on impact crater shape as impact angle decreases. Craters from top to bottom are: a) Sulpicius Gallus, b) Cauchy, c) Greaves, and d) the pair Messier and Messier A. The topography for Messier is to the upper left and for Messier A is to the lower left in (d), and profiles of Messier and Messier A are to the left and right, respectively. The scale bar in the topographic image is 5 km long. The minimum and maximum elevations shown in the topography are: Sulpicius Gallus, 3.0–5.4 km; Cauchy, 4.5–7.5 km; Greaves, 1.7–4.5 km; Messier, 3.9–6.2 km; and Messier A, 3.8–6.3 km. The lines on the imagery indicate the angle between the long axis of Messier and the plume of ejecta associated with Messier A.

the experimental data of GW78. The long ejecta streak to the WSW of Messier A does appear similar to downrange streaks observed in the experimental data for low angle impacts. However, unlike the easily visible butterfly pattern for Messier, no distal ejecta are visible in Lunar Orbiter or Clementine data in what should be the uprange and crossrange directions for Messier A. Unlike the products of experimental highly oblique impacts, the uprange and downrange rims have significant elevation. The downrange rim is as high as the crossrange rims, and the uprange rim is narrower but 200 m

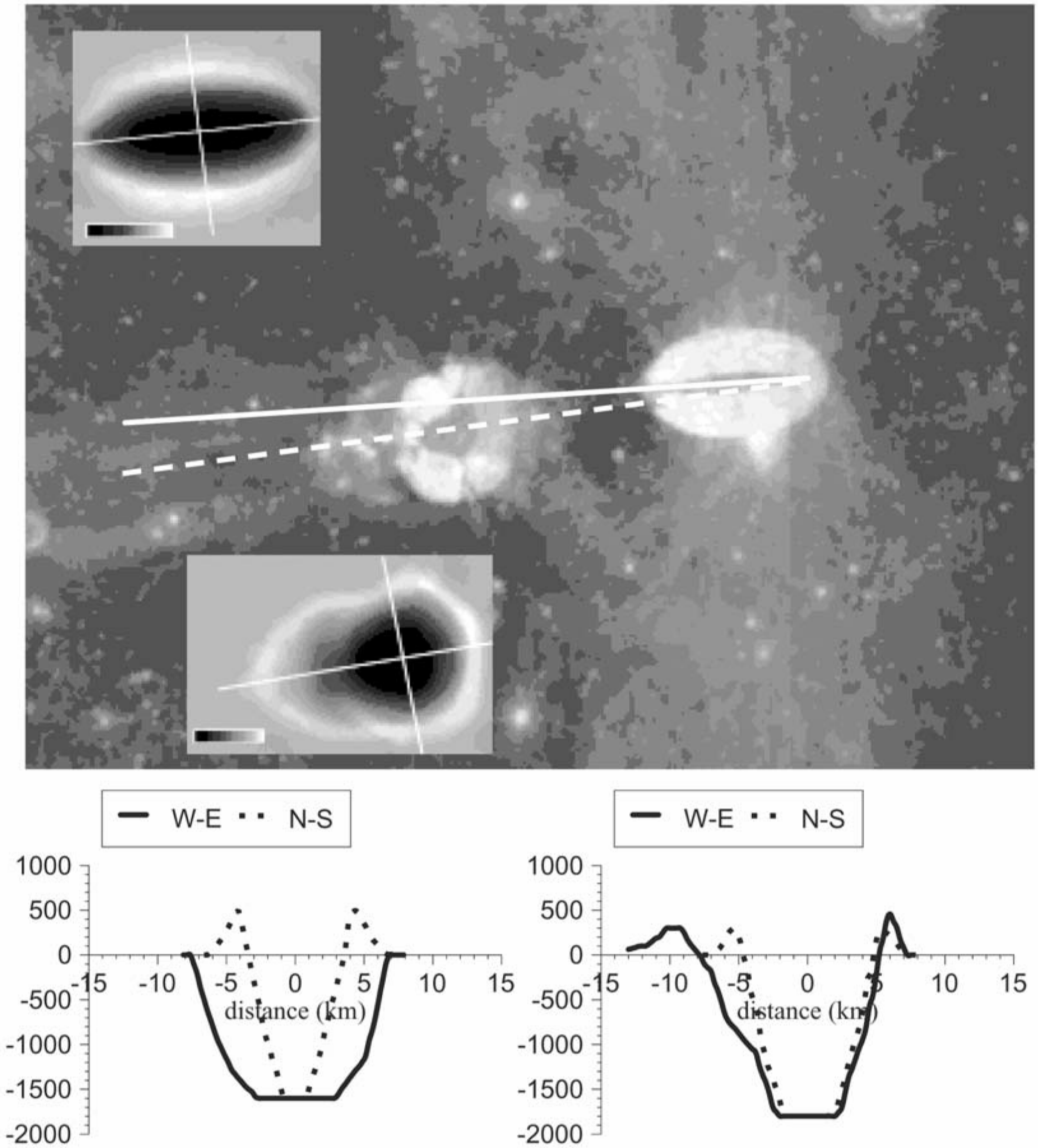

Fig. 11. Clementine imagery, LTO topography, and profiles of lunar impacts 10–15 km in diameter that show the effects on impact crater shape as impact angle decreases. Craters from top to bottom are: a) Sulpicius Gallus, b) Cauchy, c) Greaves, and d) the pair Messier and Messier A. The topography for Messier is to the upper left and for Messier A is to the lower left in (d), and profiles of Messier and Messier A are to the left and right, respectively. The scale bar in the topographic image is 5 km long. The minimum and maximum elevations shown in the topography are: Sulpicius Gallus, 3.0–5.4 km; Cauchy, 4.5–7.5 km; Greaves, 1.7–4.5 km; Messier, 3.9–6.2 km; and Messier A, 3.8–6.3 km. The lines on the imagery indicate the angle between the long axis of Messier and the plume of ejecta associated with Messier A.

higher than the crossrange rim. The floor of the crater is slightly elongated in the downrange direction. From the floors, the walls all rise at similar slopes for 600 m, and the interior slopes are similar to the other craters discussed above. Above 600 m, however, the crossrange and uprange walls continue to the rim at the same slope, but the downrange wall continues to the rim at a very shallow angle. The result is a rim planform much more elongated than the floor planform.

The shape of Messier A has some resemblance to GW78 experiments with an impact angle of 5°, where impactor decapitation causes a change of slope in the downrange direction where momentum from the impactor "blows out" the downrange wall. However, those experimental craters had no downrange or uprange rims, and the uprange wall was unusually steepened. Messier A also bears some resemblance to experimental clustered impacts (Schultz and Gault 1985). Clustered impacts at a few tens of degrees from horizontal are able to preserve an uprange and downrange rim while concentrating the majority of ejecta downrange from the crater. However, clustered impacts are more shallow than similar diameter craters resulting from a single impactor. Messier A is of similar volume to and as deep as Messier.

In summary, a logical inference, by virtue of its position, is that Messier A is a ricochet product from the impactor that produced Messier, but its shape, in many ways, does not correspond to experimental analogues of material impacting at low angles either as a cluster or single impactor. Without analogues in either experimental or planetary craters, an ad hoc explanation is required for the shape of Messier A. For example, Nyquist (1984) proposed that Messier A is a doublet crater that was fortuitously oriented along the line of the projectile that formed Messier. Doublet craters are a product of binary asteroid impact, and the amount of asteroid separation determines whether overlapping or separated craters form. Recent work has suggested that ~16% of the near-Earth asteroid population are doublets (Margot et al. 2002). Another odd property of Messier and Messier A is that the projectile direction of travel one would infer by drawing a line perpendicular to the butterfly ejecta pattern, bisecting Messier A, and through the downrange ejecta streak is at an angle of ~5° to the major axis of Messier (Fig. 11). While witness plates from experiments show significant portions of the ricochet deviating off-axis by as much as 10°, the ricocheted material is closely centered on the shot axis (GW78; Christiansen et al. 1993).

The sequence of shapes observable in the 10–15 km diameter range is applicable to both larger and smaller craters. In particular, we saw no consistent evidence for an uprange steepening of the wall at low angles, unlike the experimental data of GW78. Proclus, a crater in the highlands with an uprange forbidden zone easily discernible in imagery (Fig. 12), has enhanced wall collapse on the uprange side of the crater. This may indicate an initial oversteepening of the excavation cavity in the uprange direction, but the enhanced uprange collapse is not a feature common to oblique impacts. Torricelli (Fig. 13) is the only crater in the LTO data that mimics the experimental data for weak impactors striking the surface at ~5°, where the result is a circular crater that has one side blown out by the impactor's momentum such that the resulting planform is a teardrop shape with the point of the tear downrange and shallow.

Venusian Craters

We consider 5 different size ranges of crater diameters: 70–100 km, 40–70 km, 30–40 km, 15–30 km, and <15 km in diameter. The survey of morphologies was limited to craters >30 km in diameter to prevent a bias in the percentages from atmospheric filtering out of low angle impacts. Because our survey of the topographic structure of oblique impacts is anecdotal in nature, we have no such restriction on the size range studied. The groupings primarily represent ranges over which similar-sized craters in the categories of Fig. 8 can be found. The 2 largest size ranges are peak ring craters, and the next 2 size ranges are central peak craters. Table 5 summarizes the craters used for analysis. Herrick and Sharpton (2000) determined that most craters with radar-dark floors have experienced some level of post-impact volcanic infilling and/ or exterior embayment. Therefore, in most cases, rim-floor depths and rim heights do not reflect original crater topography and cannot be compared. For convenience, we refer to the categories illustrated in Fig. 8 as categories 1–5,

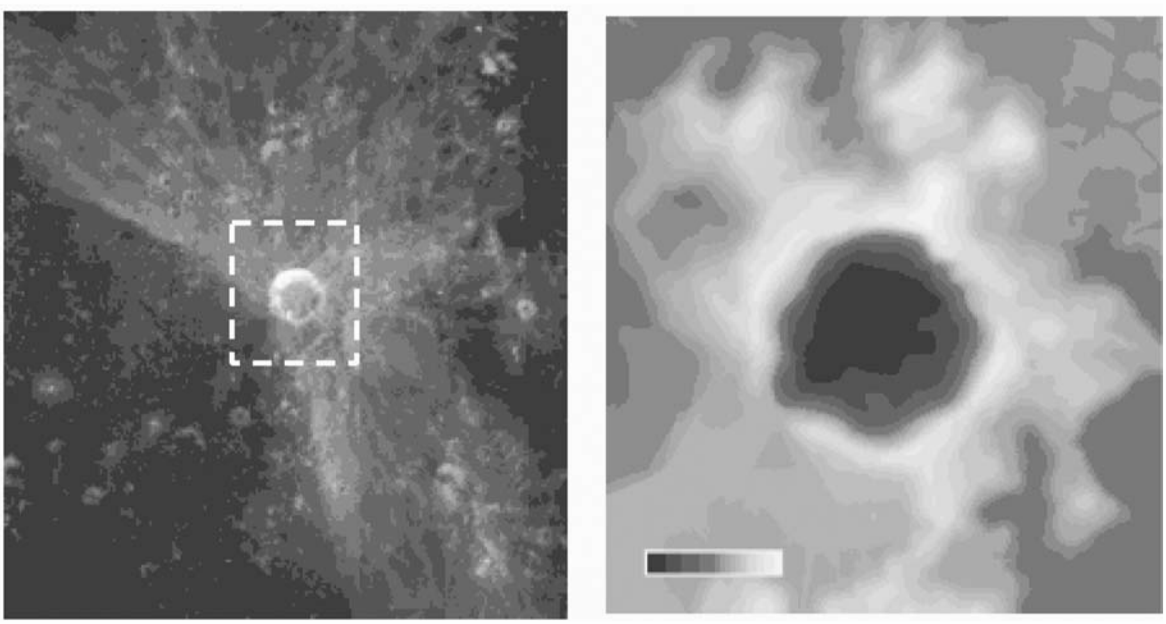

Fig. 12. Clementine imagery and LTO topography for Proclus. The scale bar is 15 km long and spans from 4.0 km to 9.0 km elevation. Proclus is located in the highlands and has a forbidden zone in the uprange direction to the SW.

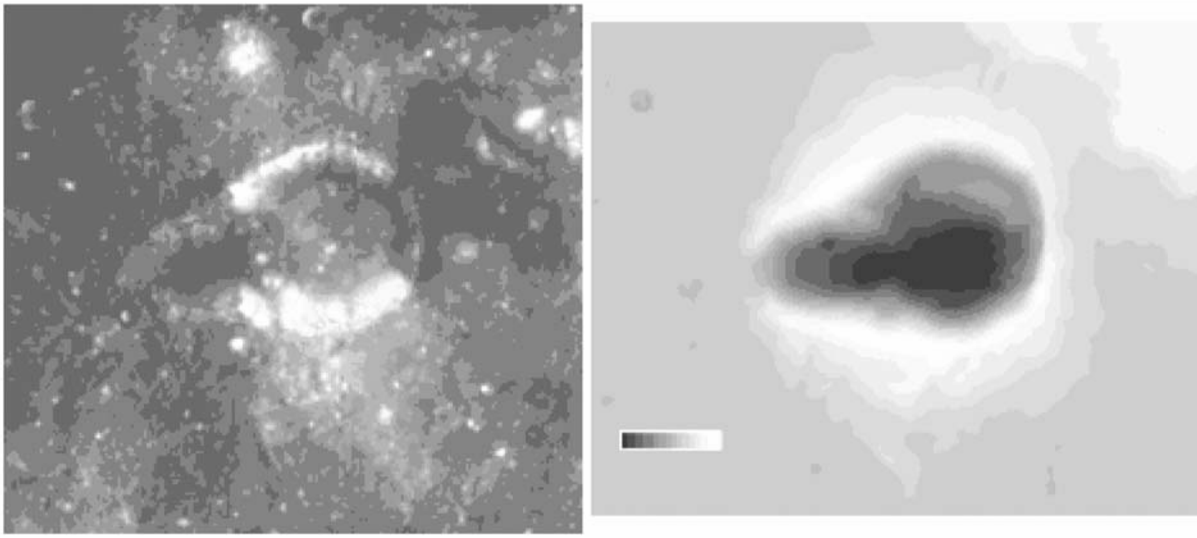

Fig. 13. Clementine imagery and LTO topography for Torricelli. The scale bar is 10 km and spans elevations of 3.0 to 6.2 km. Torricelli mimics low-angle experimental impacts with weak projectiles. In such impacts, one side of the crater is blown out by impactor momentum, and the resulting planform is a teardrop shape with the point of the tear downrange and shallow.

with Category 1 representing the most symmetric ejecta (or most near-vertical impact).

70–100 km Diameter Craters

All of the craters in this size range have peak rings and extensive terracing of the rim. Stereo coverage does not exist for any craters in this size range in the most oblique category. The rim elevations for craters in categories 1 and 2 are largely axisymmetric, and variations do not appear to be related to impact directions. Markham (4.1°S, 155.6°E, diameter 71.8 km), representative of category 3 craters, has a depressed rim to the southwest, interpreted to be the uprange direction. The depression covers ~100° of arc. The remainder of the rim is of similar elevation, roughly 300 m above the surrounding terrain. The exception is a groove in the downrange direction that covers ~20° of arc. This groove, visible in the imagery, is not a common feature of similar-sized craters with similar ejecta blankets. Regional topography around Markham shows a 1500 m drop over 500 km to the ENE of the crater in the general direction of the rather extensive ejecta flows. Marie Celeste (23.4°N, 140.4°E, diameter 96.6 km) is the most oblique of the impacts in this range with stereo coverage. Stereo coverage does not exist in the uprange direction for this crater, but the Cycle 1 imagery indicates that it does not have a rim in this direction. Coverage exists for half of the rim, and a continuous rise of 800 m exists in the rim topography from the crossrange to the downrange direction.

Topography of the peak ring does not seem to be related to impact angle for this size range. The peak ring of Marie Celeste is offset ~11 km downrange from the crater center, and the region inside the peak ring is ~200 m lower than outside the peak ring. The offset of the peak downrange is not observed for similar-sized category 4 craters. The regional topography and imagery suggest that a ridge belt buried by subsequent volcanic plains may extend under the crater and that the peak ring is centered on this feature (Fig. 14).

40–60 km Diameter Craters

Forty km is the approximate transition diameter between central peak and peak ring craters. The craters we have grouped together in the 40–60 km diameter range have either a peak ring or several isolated interior peaks. In Fig. 15, we show imagery with contoured topography for a crater in each ejecta category. None of the craters in this size range with stereo coverage have a bright floor, so assessing whether or not rim-floor depth varies with impact angle is impossible.

For category 1–3 craters, the rims are circular and their shapes do not appear to have any relationship to the impact direction. For Voynich, a category 4 crater, the rim in the uprange direction is 100–250 m below the remainder of the rim. The uprange rim of Voynich is still 100 m above the surrounding terrain. Manzolini (category 5) has a very unusual planform and topography. The crater is highly elongated with no rim elevation in either the uprange or downrange direction. The rim topography of Manzolini is best characterized as saddle-shaped, with the cross-range rim about 300 m higher than the surrounding terrain. Manzolini has a small, incomplete peak ring that is offset by 5 km in the uprange direction relative to the rim. Its central structure rises to nearly the level of the uprange and downrange rim. In contrast, for category 1–3 craters, the central structure elevation is ~600 m below the rim. The unusual thing about Manzolini is that close inspection shows that the overall structure seems to be superposed on a much more circular structure centered on the interior ring (Fig. 15). A speculative

Table 5. Summary of venusian craters used for analysis of crater shape.

Name	Latitude	Longitude	Diameter	Ejecta category
70–100 km diameter				
Greenaway	22.9°	145.1°	92.3 km	1
Potanina	89.6	31.7	53.0	1
Stowe	–43.2	233.2	75.3	2
Markham	–4.1	155.6	71.8	3
Marie Celeste	23.4	140.4	96.6	4
40–70 km diameter				
Corpman	0.3	151.8	45.1	1
Cori	25.4	72.9	54.7	2
Carreno	–3.9	16.1	56.8	3
Voynich	35.3	56.1	47.9	4
Manzolini	25.7	91.3	43.7	5
30–40 km diameter				
Xantippe	–10.9	11.7	40.6	1
Agripinna	–33.3	65.7	38.4	2
Bassi	–19.0	64.7	31.4	2
Ban Zhao	17.2	146.9	38.3	3
Germain	–38.0	63.7	35.9	3
Bourke-White	21.2	147.9	34.4	3
15–30 km diameter				
Riley	14.0	72.5	18.8	1
Li Quingzhao	23.7	94.6	22.4	2
Ma Shouzen	–35.7	92.5	18.3	2
Adivar	8.9	76.2	29.0	3
Konopnicka	14.5	166.6	19.9	3
Budevska	0.5	143.2	18.7	3
0–15 km diameter				Description
Kylli	41.1	67.0	12.8	Circular, symmetric ejecta
Phyllis	12.2	132.4	10.6	Circular, symmetric ejecta
Parishan	–0.2	146.5	6.4	Circular, symmetric ejecta
Katusha	–28.6	60.0	12.7	Circular, asymmetric ejecta
Ualinka	13.2	168.6	8.1	Circular, asymmetric ejecta
Avene	40.4	149.4	11.0	Multiple-floored
Oshalche	29.7	155.6	9.6	Multiple-floored
Loan	28.2	60.0	7.8 and 4.2	Crater field
Nsele	6.7	64.2	4.8 and 2.1	Crater field
unnamed	5.8	84.3	4.8	Largest crater in field
Dheepa	–21.6	176.3	4.7 and 1.5	Crater field

explanation is that Manzolini shows the effects of downrange impactor ricochet superposed on the primary structure. In this interpretation, the downrange rim of what would otherwise be a fairly circular complex crater has been distorted by ricochet material. The larger crater Graham (110 km × 47 km, Fig. 16), not covered in stereo imagery, appears to be the only true venusian analogue to Messier.

30–40 km Diameter Craters

Stereo coverage is not available for any impact craters in this size range for the 2 most oblique categories. The craters in categories 2 and 3 have rims with topography that is symmetric around the perimeters, and the central peaks are centered within the rims. Central peak elevations for this size range do not have a relationship to impact angle. For example, 2 of the craters in category 3, Ban Zhao and Bourke-White, have central peaks that rise to the level of the rim, while Germain, which has a similar ejecta blanket, has a central peak 500 m below the rim.

Xantippe (Fig. 17), the ejecta blanket of which is consistent with the near-vertical category (Category 1), is the only crater in this size range with an asymmetric rim and a central peak not centered within the rim. Flows of the ejecta suggest that the downrange direction may have been to the southwest. The rim topography rises continuously from 50–100 m above the surrounding terrain northeast of the crater to ~400 m to the southwest. Xantippe is located in a structurally complex area near an embayed tessera unit. Xantippe may have formed with axisymmetric rim topography and then was subsequently tilted, or perhaps subsurface structure can

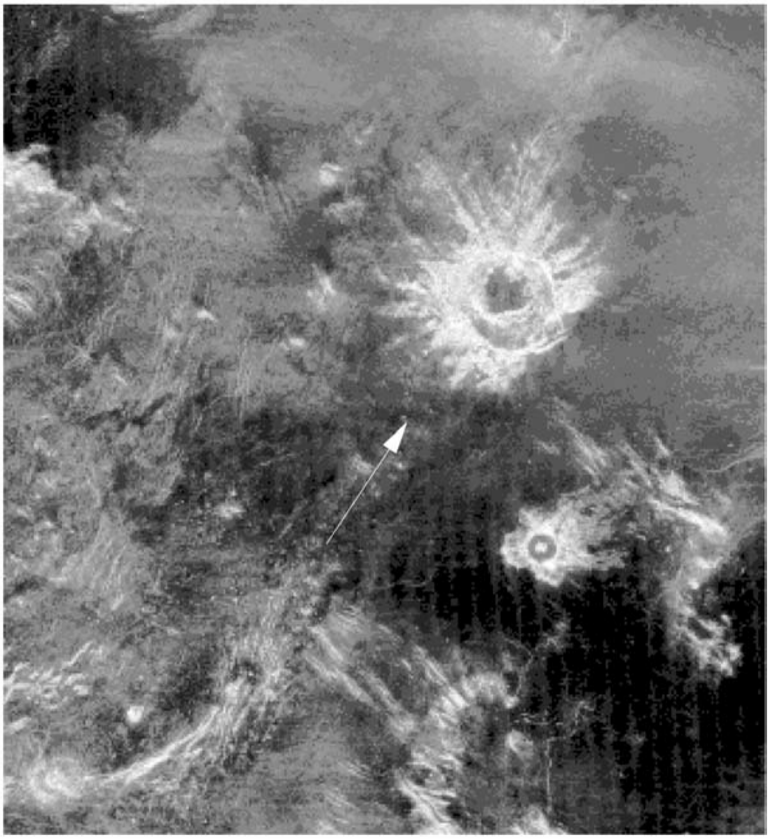

Fig. 14. Regional Magellan image of Marie Celeste crater (97 km diameter), with the arrow showing the extension of a linear tectonic/volcanic feature that may have influenced the formation of the crater.

account for the unusual property of a symmetric ejecta blanket with asymmetric rim properties.

15–30 km Diameter Craters

All the craters we analyzed in this diameter range have a single central peak. In this size range, stereo coverage was not available for any impact craters in the 2 most oblique categories. The 3 craters analyzed in categories 1 and 2 all had axisymmetric rim topography. We analyzed 3 craters that were in category 3. For 2 of these craters, Adivar and Budevska, the rim topography is axisymmetric. The rim of Konopnicka, however, is ~200 m lower than the remainder of the rim over ~20° of arc in the uprange direction. For all the craters near 20 km in diameter, the central peak is relatively small and rises to 400–500 m below the rim.

Craters <15 km in Diameter

The planform and shape of impact craters in this size range should be affected by 2 distinctly different phenomena, oblique impact and meteoroid disruption. Meteoroids entering the venusian atmosphere are disrupted by aerodynamic drag forces. The meteoroid will deform and break apart upon entry, and small meteoroids, apparently, will explode in the atmosphere so that no craters below ~2 km in diameter form on Venus (Tauber and Kirk 1976; Ivanov et al. 1986). For larger meteoroids, the fragments will disperse. For craters below ~20 km in diameter, the separation of fragments can be large enough to create crater fields or a crater with an irregular planform and "multiple floors" (Phillips et al. 1991; Phillips et al. 1992; Herrick and Phillips 1994). A loose correlation should exist between impact angle and fragment dispersal, as a more horizontal impact angle results in a longer path length through the atmosphere and more time for the fragments to separate.

The combination of fragment dispersal and the effects of oblique impact create a wide variety of impact structures at small diameters. We divide the craters in this size range into 4 categories that should loosely indicate progressively more horizontal impact angles: near-vertical impacts, oblique impacts, multiple-floored craters, and crater fields. Near-vertical impacts are circular with an axisymmetric ejecta blanket. Oblique impacts are craters with a circular planform but an asymmetric ejecta blanket. Multiple-floored craters have an irregular planform and an interior that appears to result from multiple meteoroid fragments striking the surface. Crater fields result from the simultaneous impact of multiple meteoroid fragments that are separated enough to form individual craters. We have stereo coverage for at least 2 craters in each of these categories.

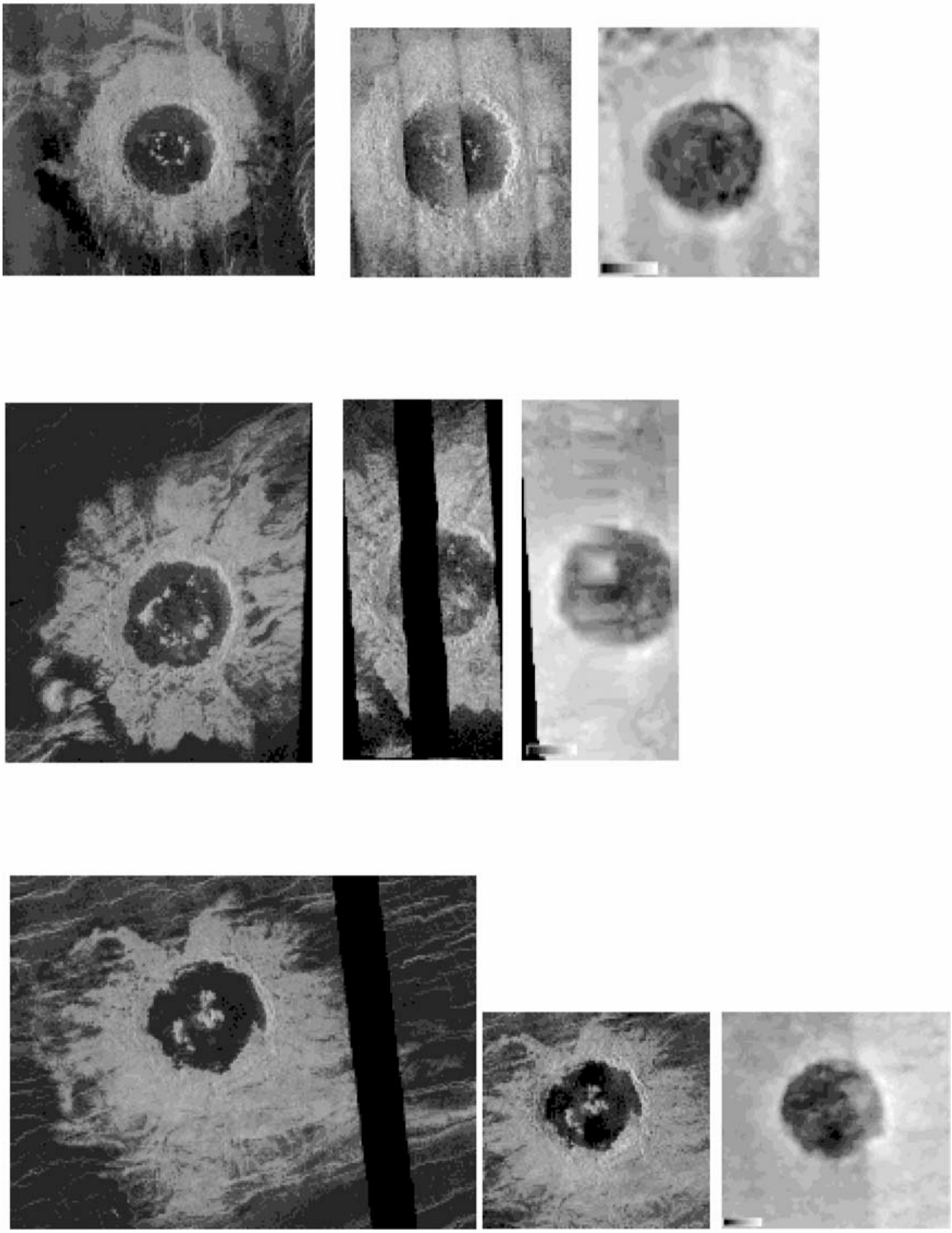

Fig. 15. Venusian craters 40–60 km in diameter that show increasing ejecta asymmetry. For each crater, from left to right is the cycle 1 Magellan imagery, an orthorectified version of the cycle 3 imagery that matches in area the stereo-derived topography coverage, and the topography as a grayscale image. The scale bar in the topography images is 20 km long and spans 1500 m of elevation. In some cases, the image mosaicing process has introduced obvious step functions in the stereo-derived topography; these are ignored in data interpretation. The craters are: a) Corpman (45 km diameter), b) Cori (55 km), c) Carreno (57 km), d) Voynich (48 km), and e) Manzolini (44 km). Note that while the interior of Manzoli seems highly elongated in planform, the rim is much more circular (dotted line).

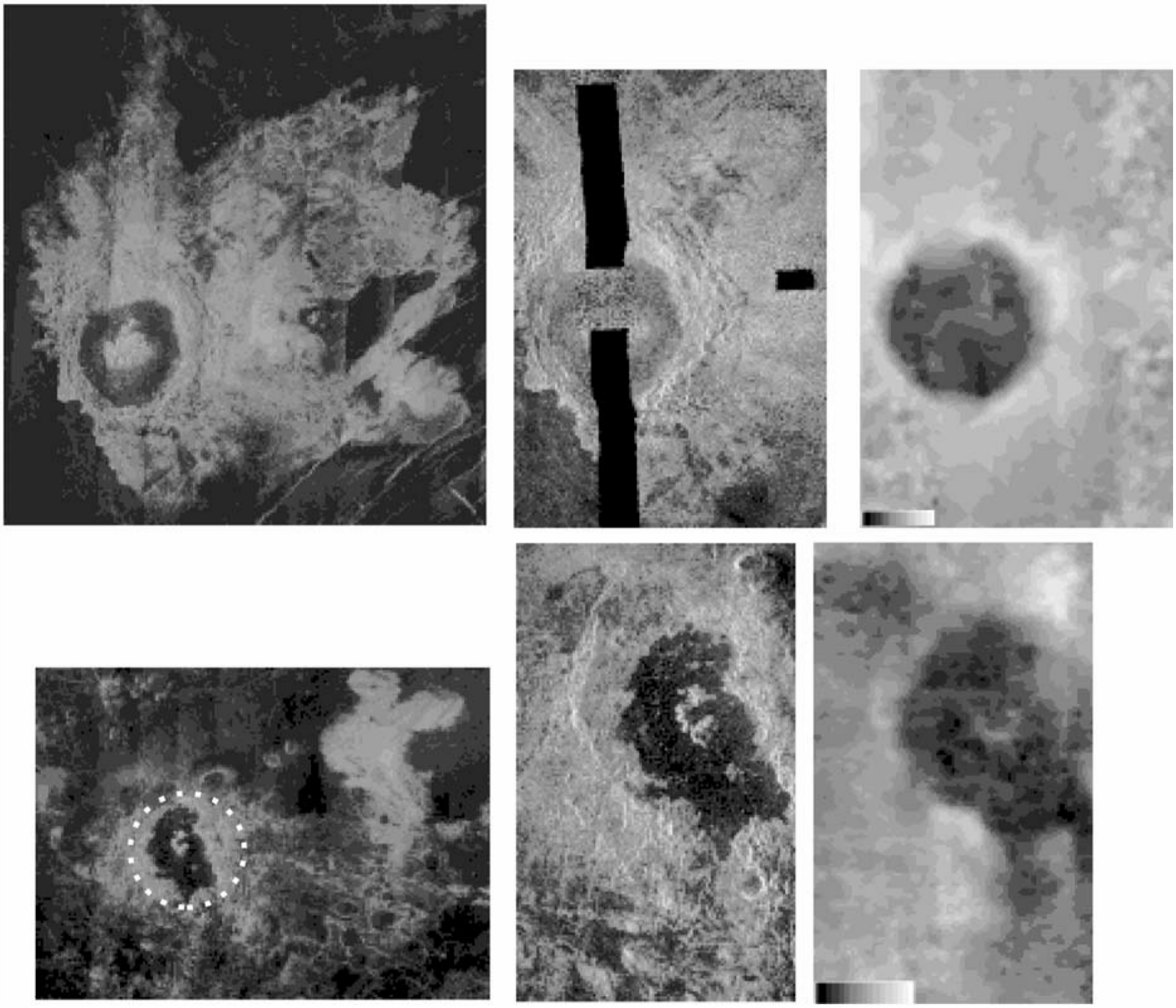

Fig. 15. Venusian craters 40–60 km in diameter that show increasing ejecta asymmetry. For each crater, from left to right is the cycle 1 Magellan imagery, an orthorectified version of the cycle 3 imagery that matches in area the stereo-derived topography coverage, and the topography as a grayscale image. The scale bar in the topography images is 20 km long and spans 1500 m of elevation. In some cases, the image mosaicing process has introduced obvious step functions in the stereo-derived topography; these are ignored in data interpretation. The craters are: a) Corpman (45 km diameter), b) Cori (55 km), c) Carreno (57 km), d) Voynich (48 km), and e) Manzolini (44 km). Note that while the interior of Manzoli seems highly elongated in planform, the rim is much more circular (dotted line).

All of the craters in this size range have little or no interior filling, so we can compare rim-floor depths between craters. The general trend is of decreasing rim-floor depth with the progression from single, near-vertical impacts to the individual craters of crater fields. Figure 18 shows rim-floor depths versus diameter for craters in each of the 4 categories, and Fig. 19 shows profiles for Parishan (0.2°S, 146.5°E) and an unnamed crater at 5.8°N, 84.3°E. The former is an isolated 6.4 km diameter crater with an axisymmetric ejecta blanket, and the latter is a 4.8 km diameter crater within a crater field. Our interpretation is that the progression results from increasing dispersion of the impacting material for multiple-floored craters and individual craters within a crater field. These craters are formed from "clustered impacts," which reduce the cratering efficiency for a given impactor mass and results in a shallower crater (Shultz and Gault 1985).

The rim topography and ejecta planforms of craters in this size range are also consistent with combinations of the effects of impactor dispersal and impact angle (Fig. 20). The rim topography is axisymmetric for the near-vertical impacts. Ualinka (13.2°N, 168.6°E; Fig. 20a) can be interpreted as an oblique impact with minimal impactor dispersion. The rim topography appears saddle-shaped, and ejecta are concentrated in the cross-range directions. In contrast, the multiple-floored craters we analyzed have highly irregular planforms indicative of a clustered impact, but their rim topography has no asymmetry that is obviously attributable to impact direction. Oshalche (29.7°N, 155.5°E; Fig. 20b) has a highly asymmetric ejecta blanket with ejecta concentrated in the crossrange and

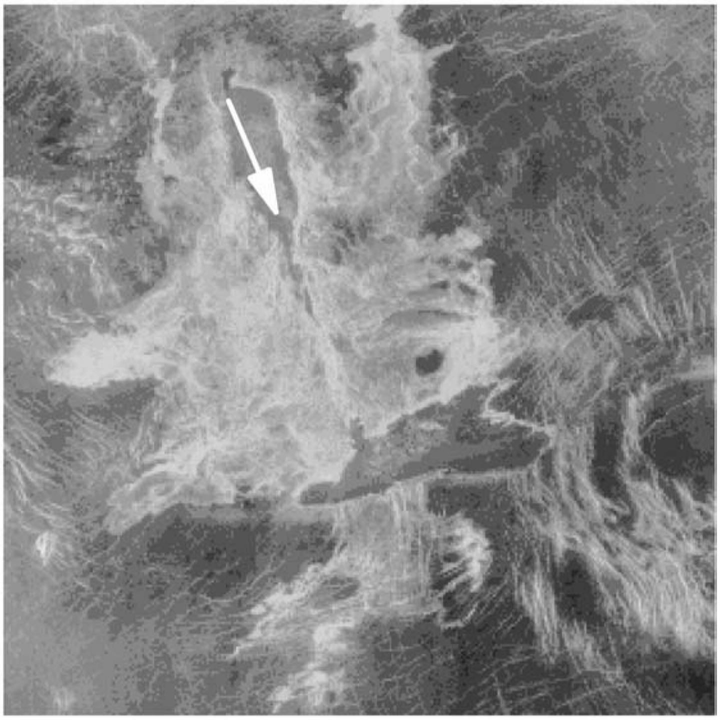

Fig. 16. Graham crater (110 × 47 km) is the largest example on Venus of a highly elongated impact structure likely to have resulted from a grazing impact.

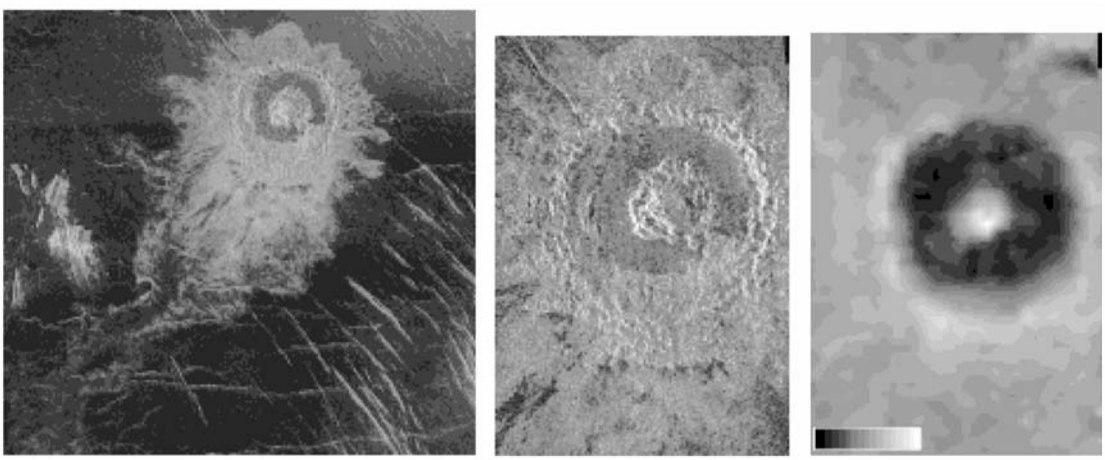

Fig. 17. The scale bar in the topography images is 20 km and spans 1500 m of elevation. Xantippe crater (41 km diameter) has a symmetric ejecta blanket but asymmetric rim topography; the rim increases in elevation from north to south. Because the region appears to have had a complex volcanic and tectonic history, Xantippe may have had asymmetric rim topography when it formed and then was subsequently tilted. From left to right is the cycle 1 Magellan imagery, an orthorectified version of the cycle 3 imagery that matches in area the stereoderived topography coverage, and the topography as a grayscale image.

downrange direction, but its rim is of fairly constant elevation around its perimeter. This is consistent with observations of clustered impacts with modest dispersion and an impact angle of 45° in the experiments of Schultz and Gault (1985; Fig. 17b, second to last image). The individual craters within the crater fields for which we have topography are consistent with experiments showing oblique clustered impacts with greater impactor dispersion (Schultz and Gault 1985; Fig. 17b). The ejecta are concentrated in the downrange and crossrange directions, the uprange rim has negligible topography, and the downrange and crossrange rims are similar in elevation.

Summary of Topography Observations

The progression of rim shape for venusian craters of more than ~20 km in diameter is similar to that for lunar

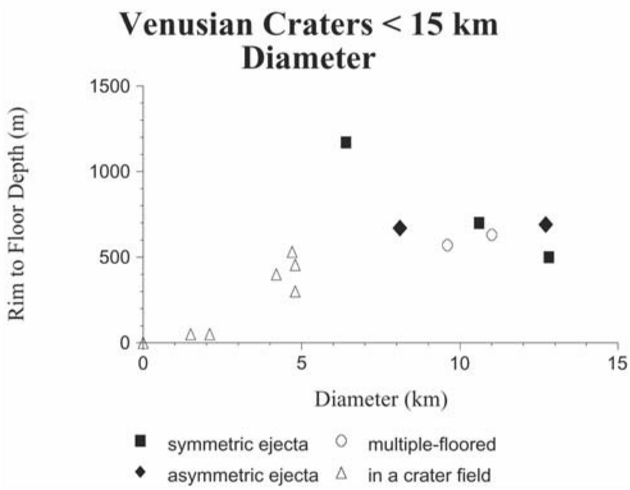

Fig. 18. Rim-floor depths (calculated as in Herrick and Sharpton [2000]) versus diameter for several craters <15 km in diameter. Although the data is anecdotal, there seems to be a progression of shallower depths for craters with greater spread of impactor fragments.

craters. As impact angle decreases, the uprange rim becomes depressed, and then, the topography progresses to a saddle-shaped topography. The transition from a symmetric rim to a depressed uprange rim occurs in craters with ejecta blankets in category 3, or those with a notch in the ejecta blanket. In other words, a forbidden zone is required in the uprange direction before the uprange rim becomes depressed. If a $\sin^2\Theta$ dependence of cumulative crater percentage versus impact angle is assumed, then a depressed uprange rim occurs at ~40–45° from horizontal.

Not enough examples exist to estimate the angular occurrence of the transition to saddle-shaped topography. No evident correlation exists between impact angle and the shape or location of a crater's central peak or peak ring. For smaller craters, a wide variety of crater shapes and rim shapes exist that are consistent with experiments from both oblique and clustered impacts (GW78; Schultz and Gault 1985). In these smaller craters and crater fields, the general trend is of decreasing depth versus diameter with increasing separation of impactor fragments.

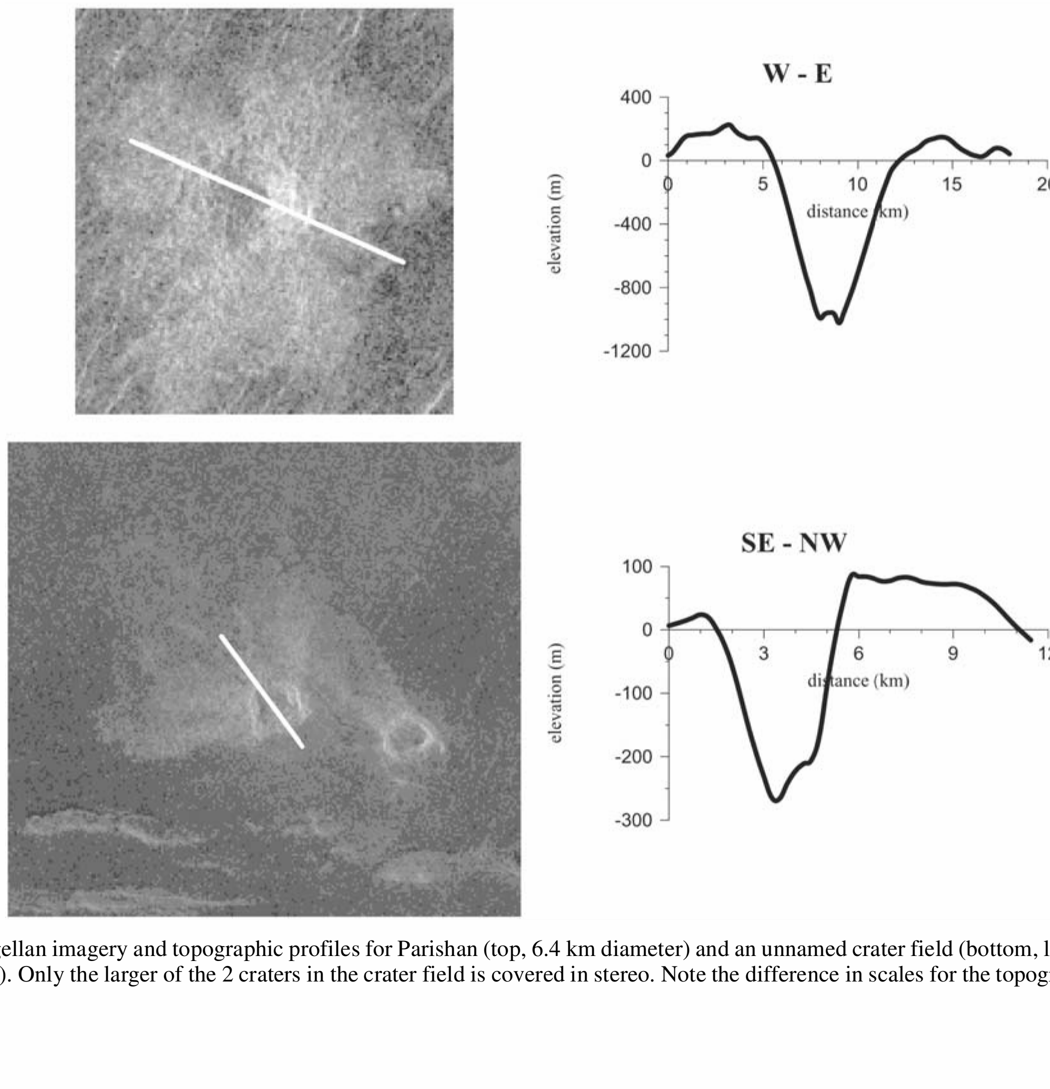

Fig. 19. Magellan imagery and topographic profiles for Parishan (top, 6.4 km diameter) and an unnamed crater field (bottom, larger crater 4.8 km diameter). Only the larger of the 2 craters in the crater field is covered in stereo. Note the difference in scales for the topographic profiles.

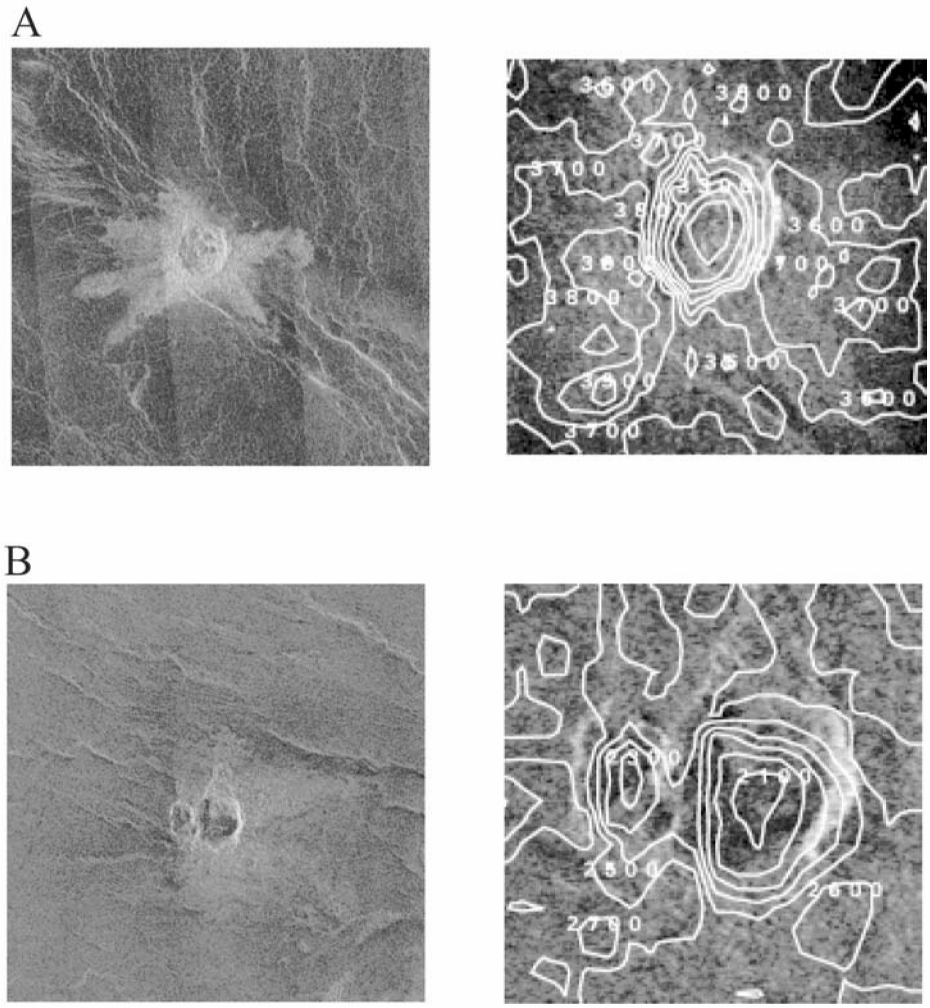

Fig. 20. Magellan imagery and contoured topography for (a) Ualinka (13.2°N, 168.6°E, 8 km diameter) and (b) Oshalche (29.7°N, 155.5°E, 9 km diameter). Ualinka is interpreted as a low angle impact with minimal impactor dispersion. Oshalche is consistent with a higher impact angle and greater impactor dispersion.

DISCUSSION

The progressions of ejecta pattern and interior shape with decreasing impact angle are mostly consistent with what is expected from laboratory and theoretical work. The inferred impact angles show no compelling evidence that cratering efficiency is strongly dependent on impact angle, but the error bars on our surveys are large enough that such a dependence cannot be ruled out. On both Venus and the Moon, the ejecta blanket becomes asymmetric at higher inferred impact angles than the rim. This observation is consistent with the idea that the ejecta curtain is initially asymmetric for oblique impacts but becomes more symmetric as the excavation process continues. The progression of rim shape with decreasing impact angle for both planets is as follows: first, the uprange rim decreases in height while the crossrange and downrange rims retain the same height; as the impact angle continues to decrease, the downrange rim also decreases in elevation; and, at the lowest impact angles, the planform becomes elliptical. Except for smaller impacts on Venus (discussed below), no evidence exists that the depth versus diameter relation changes with impact angle.

Some aspects of crater shape are not consistent with or not predicted by laboratory work. In the lunar craters, no variation occurs in interior slope within oblique impacts, and no changes in interior slope occur as the impact angle decreases. For elliptical craters, the absolute difference between the major and minor axes remains constant from floor to rim, so the rim is less elliptical than the floor. For circular craters, the excavated volume of material remains constant, but the crossrange rims become thicker (but not higher) as the uprange and then downrange rims decrease in elevation. The 2 possible interpretations of the constant slopes are that the transient cavity of a crater retains the same basic shape regardless of impact angle or that post-impact slumping equalizes interior slopes regardless of initial conditions. The constancy in slope occurs down to the smallest crater sizes analyzed (5 km diameter). These smallest craters are clearly simple craters and show no obvious signs of significant interior slumping. Thus, our favored interpretation is a constant transient cavity shape regardless of impact angle. This is not consistent with the experimental impacts of GW78.

The presence of an atmosphere makes venusian impact craters different from those on the Moon. As predicted from experimental work (Schultz 1992b, c), all effects associated with oblique impact occur at higher impact angles, and a forbidden zone in the ejecta never develops downrange. Smaller impacts on Venus show shape characteristics consistent with clustered impact experiments (Schultz and Gault 1985), particularly, a general decrease in depth versus diameter with increasing fragment separation.

Differences exist between the expected angles for which certain phenomena occur and the angles inferred from the crater surveys shown in Tables 2–4. Our findings for the most oblique impacts match well with the work of Bottke et al. (2000). They found that ~5% of the impact craters on Venus and the Moon have highly elliptical planforms. We found that similar percentages of craters on the Moon have saddle-shaped topography and butterfly ejecta patterns, and about the same percentage of venusian craters have fly-wing ejecta patterns. These percentages are far higher than those predicted by the experiments of GW78 and indicate that these phenomena must occur at higher impact angles on the planets than in the experiments. Bottke et al. (2000) attributed the discrepancy to a higher projectile-to-crater diameter ratio for planetary impacts relative to the experiments of GW78. The higher ratio can be caused by differences in a variety of parameters (e.g., target density, projectile density, projectile velocity, material properties) between experimental and planetary impacts. Bottke et al. (2000) described the impactor footprint as an ellipse with ellipticity of 1/sinΘ. A lower impact angle is required in the experiments to make the absolute difference in the semi-major versus semi-minor axis for the impactor footprint significant compared to the crater diameter.

Bottke et al.'s (2000) hypothesis, however, cannot be extended to all oblique impact phenomena. CosΘ, the derivative of sinΘ, decreases with increasing impact angle. If the onset of all oblique impact phenomena (angle at which the forbidden zone occurs, etc.) were dependent on the ellipticity of the impactor footprint versus transient crater diameter, then the discrepancy of onset angles between experimental and planetary data would increase for the phenomena that occur at higher angles. We observe that the higher angle phenomena, such as an uprange depressed rim and forbidden zone, occur at similar angles in the planetary and experimental data. In the experimental data of GW78, the transition to noncircular craters is highly dependent on projectile and target properties (Figs. 1 and 2 of GW78), while for all strengthless targets, the displaced mass versus impactor mass is indepedent of target and projectile composition. Pierazzo and Melosh (2000) observed, in numerical simulations, that the volume pressure decay constant becomes much lower at impact angles less than 30°, which means a slower decay of the shock wave away from the point of impact. If the threshold to a lower decay constant is material dependent, that may explain why discrepancies between experimental and planetary data are significant only at the lowest angles.

Acknowledgments–This work has benefited from discussions with Buck Sharpton, Paul Spudis, and Ben Bussey. Chris Cochrane pointed out the underlying circular structure in Manzolini. Useful comments were provided by Bill Bottke and an anonymous reviewer. The complete data sets used in the surveys are available from Robert Herrick upon request. This is LPI Contribution 1193.

Editorial Handling—Dr. Wolf Uwe Reimold

REFERENCES

Anderson J. L. B., Schultz P. H., and Heineck J. T. 2000. The effects of impact angle on the shape of lunar craters (abstract #1749). 31st Lunar and Planetary Science Conference. CD-ROM.

Barlow N. G. and Bradley T. L. 1990. Martian impact craters: Correlations of ejecta and interior morphologies with diameter, latitude, and terrain. *Icarus* 87:156–179.

Bottke W. F., Love S. G., Tytell D., and Glotch T. 2000. Interpreting the elliptical crater populations on Mars, Venus, and the Moon. *Icarus* 145:108–121.

Christiansen E. L., Cykowski E., and Ortega J. 1993. Highly oblique impacts into thick and thin targets. *International Journal of Impact Engineering* 14:157–168.

Cintala M. J., Berthoud L., and Hörz F. 1999. Ejection-velocity distributions from impacts into coarse-grained sand. *Meteoritics & Planetary Science* 34:605–623.

Cook A. C., Robinson M. S., and Watters T. R. 2000. Planet-wide lunar digital elevation model (abstract #1978). 31st Lunar and Planetary Science Conference. CD-ROM.

Ekholm A. G. and Melosh H. J. 2001. Crater features diagnostic of oblique impacts: The size and position of the central peak. *Geophysical Research Letters* 28:623–626.

Gault D. E. and Wedekind J. A. 1978. Experimental studies of oblique impact. Proceedings, 9th Lunar and Planetary Science Conference. pp. 3843–3875.

Hartmann W. K. 1999. Martian cratering VI: Crater count isochrons and evidence for recent volcanism from Mars Global Surveyor. *Meteoritics & Planetary Science* 34:167–178.

Herrick R. R. and Phillips R. J. 1994. Effects of the venusian atmosphere on incoming meteoroids and the impact crater population. *Icarus* 112:253–281.

Herrick R. R. and Sharpton V. L. 2000. Implications from stereo-derived topography of venusian impact craters. *Journal of Geophysical Research* 105:20245–20262.

Hörz F., Grieve R., Heiken G., Spudis P., and Binder A. 1991. Lunar surface processes. In *Lunar sourcebook,* edited by Heiken G. H., Vaniman D. T., and French B. M. Cambridge: Cambridge University Press. pp. 61–120.

Housen K. R., Schmidt R. M., and Holsapple K. A. 1983. Crater ejecta scaling laws: Fundamental forms based on dimensional analysis. *Journal of Geophysical Research* 88:2485–2499.

Ivanov B. A. 1990. Venusian impact craters on Magellan images: View from Venera 15/16. *Earth, Moon, and Planets* 50/51:159–173.

Ivanov B. A., Basilevsky A. T., Kryuchkov V. P., and Chernaya I. M. 1986. Impact craters of Venus: Analysis of Venera 15 and 16 data. *Journal of Geophysical Research* 91:D413–D430.

Johnson R. R. 1973. *Elementary statistics.* North Scituate: Duxbury Press. 480 p.

Margot J. L., Nolan M. C., Benner L. A. M., Ostro S. J., Jurgens R. F., Giorgini J. D., Slade M. A., and Campbell D. B. 2001. Binary asteroids in the near-Earth object population. *Science* 296:1445–1448.

McKinnon W. B., Zahnle K. J., Ivanov B. A., and Melosh H. J. 1997. Cratering on Venus: Models and observations. In *Venus II,* edited by Bougher S. W., Hunten D. M., and Phillips R. J. Tucson: University of Arizona Press. pp. 969–1014.

Melosh 1989. *Impact cratering: A geologic process.* New York: Oxford University Press. 245 p.

Nozette S., Rustan P., Pleasance L. P., Horan D. M., Regeon P., Shoemaker E. M., Spudis P. D., Acton C. H., Baker D. N., Blamont J. E., Buratti B. J., Corson M. P., Davies M. E., Duxbury T. C., Eliason E. M., Jaksoky B. M., Kordas J. F., Lewis I. T., Lichtenberg C. L., Lucey P. G., Malaret E., Massie M. A., Resnick J. H., Rollins C. J., Park H. S., McEwen A. S., Priest R. E., Pieters C. M., Reisse R. A., Robinson M. S., Simpson R. A., Smith D. E., Sorenson T. C., Vorden Breugge R. W., and Zuber M. T. 1994. The Clementine mission to the Moon: Scientific overview. *Science* 266:1835–1839.

Nyquist L. E. 1984. The oblique impact hypothesis and relative probabilities of lunar and martian meteorites. Proceedings, 14th Lunar and Planetary Science Conference. *Journal of Geophysical Research* 89:B631–B640.

Phillips R. J., Schaber G. G., Arvidson R. E., Boyce J. M., Campbell D. B., Guest J. E., and Soderblom L. A. 1991. Initial analysis of Venus impact craters with Magellan data. *Science* 252:288–297.

Phillips R. J., Raubertas R. F., Arvidson R. E., Sarkar I. C., Herrick R. R., Izenberg N., and Grimm R. E. 1992. Impact crater distribution and the resurfacing history of Venus. *Journal of Geophysical Research* 97:15923–15948.

Pierazzo E. and Melosh H. J. 2000. Understanding oblique impacts from experiments, observations, and modeling. *Annual Review of Earth and Planetary Sciences* 28:141–167.

Pike R. J. 1980. *Geometric interpretation of lunar craters.* Washington D. C.: U. S. Government Printing Office. Geological Survey Professional Paper 1046-C, NASA SP-362. 77 p.

Schmidt R. M. 1980. Meteor crater—Implications of centrifuge scaling. Proceedings, 11th Lunar and Planetary Science Conference. pp. 2099–2128.

Schultz P. H. 1976. *Moon morphology.* Austin: University of Texas Press. 626 p.

Schultz P. H. 1992a. Atmospheric effects on cratering efficiency. *Journal of Geophysical Research* 97:975–1006.

Schultz P. H. 1992b. Atmospheric effects on ejecta emplacement. *Journal of Geophysical Research* 97:11623–11662.

Schultz P. H. 1992c. Atmospheric effects on ejecta emplacement and crater formation on Venus from Magellan. *Journal of Geophysical Research* 97:16183–16248.

Schultz P. H. and Gault D. E. 1985. Clustered impacts: Experiments and implications. *Journal of Geophysical Research* 90:3701–3732.

Schultz P. H. and Lutz-Garihan A. B. 1982. Grazing impacts on Mars: A record of lost satellites. Proceedings, 13th Lunar and Planetary Science Conference. *Journal of Geophysical Research* 87:A84–A96.

Schultz P. H., Heineck J. T., and Anderson J. L. B. 2000. Using 3-D PIV in laboratory impact experiments (abstract #1902). 31st Lunar and Planetary Science Conference. CD-ROM.

Sharpton V. L. 1994. Evidence from Magellan for unexpectedly deep complex craters on Venus. In *Large meteorite impacts and planetary evolution,* edited by Dressler B. O., Grieve R. A. F., and Sharpton V. L. Boulder: Geological Society of America. Special Paper 293. pp. 19–27.

Shoemaker E. M. 1962. Interpretation of lunar craters. In *Physics and astronomy of the Moon,* edited by Kopal Z. New York: Academic Press. pp. 283–351.

Shoemaker E. M. and Wolfe R. F. 1982. Cratering time scales for the Galilean satellites. In *Satellites of Jupiter,* edited by Morrison D. Tucson: University of Arizona Press. pp. 277–339.

Tauber M. E. and Kirk D. B. 1976. Impact craters on Venus. *Icarus* 28:351–357.

Zuber M. T., Smith D. E., Lemoine F. G., and Neumann G. A. 1994. The shape and internal structure of the Moon from the Clementine mission. *Science* 266:1839–1843.